RCS COMPUTATIONS WITH PO/PTD FOR CONDUCTING AND IMPEDANCE OBJECTS MODELED AS LARGE FLAT PLATES

A THESIS

SUBMITTED TO THE DEPARTMENT OF ELECTRICAL AND

ELECTRONICS ENGINEERING

AND THE INSTITUTE OF ENGINEERING AND SCIENCES

OF BILKENT UNIVERSITY

IN PARTIAL FULFILLMENT OF THE REQUIREMENTS

FOR THE DEGREE OF

MASTER OF SCIENCE

By

N. A. Albayrak

July 2005

I certify that I have read this thesis and that in my opinion it is fully adequate, in scope and in quality, as a thesis for the degree of Master of Science.

Prof. Dr. Ayhan Altıntaş (Supervisor)

I certify that I have read this thesis and that in my opinion it is fully adequate, in scope and in quality, as a thesis for the degree of Master of Science.

Asst. Prof. Dr. Vakur B. Ertürk

I certify that I have read this thesis and that in my opinion it is fully adequate, in scope and in quality, as a thesis for the degree of Master of Science.

Prof. Dr. Gülbin Dural

Approved for the Institute of Engineering and Sciences:

Prof. Dr. Mehmet Baray
Director of Institute of Engineering and Sciences

ABSTRACT

RCS COMPUTATIONS WITH PO/PTD FOR CONDUCTING AND IMPEDANCE OBJECTS MODELED AS LARGE FLAT PLATES

N. A. Albayrak

M.S. in Electrical and Electronics Engineering

Supervisor: Prof. Dr. Ayhan Altıntaş

July 2005

Calculation of Radar Cross Section (RCS) of arbitrary bodies using Physical Optics (PO) Theory and Physical Theory of Diffraction (PTD)is considered. For bodies with impedance surface boundary condition, only PO is used. Analytical approach to PO integral is used to achieve faster computations. A computer program has been developed in Fortran in order to calculate the Radar Cross Section (RCS). Arbitrary shape is modeled as triangular facets of any area by the help of graphical tools. Given the triangular meshed model of an arbitrary body, Physical Optics(PO) surface integral is numerically evaluated over the whole surface. There is no limitation on the size of the triangles, as soon as the total surface does not retire from the original one.

Shadowing algorithm has been used in order to have more accurate solutions. Additionally, flash points of PO are visualized over the surface of targets, hence local nature of high-frequency phenomena is proved.

Induced surface currents, edge currents and RCS have been calculated for some basic shapes and the fuel tank model of F-16 airplanes. Induced surface currents have been visualized over the surface of the particular targets using Matlab.

Keywords: Physical Optics (PO), RCS, Radar Cross Section, Impedance Surface, Flat Plate Modeling, Triangular Flat Plates, Physical Theory of Diffraction (PTD).

ÖZET

FİZİKSEL KIRINIM TEORİSİ İLE BÜYÜK PLAKALARLA MODELLENMİŞ İLETKEN VE EMPEDANS CİSİMLERİN RADAR KESİT ALANI HESAPLANMASI

N. A. Albayrak
Elektrik ve Elektronik Mühendisliği Bölümü Yüksek Lisans
Tez Yöneticisi: Prof. Dr. Ayhan Altıntaş
Temmuz 2005

Fiziksel Optik Yöntemi ve Kırınımın Fiziksel Teorisi kullanılarak iletken ve empedans yüzeyler için Radar Kesit Alanı hesaplanmıştır. Hesaplamaları hızlandırabilmek için PO integrali analitik olarak hesaplanmıştır. Herhangi bir cismin Radar Kesit Alanını hesaplamak için Fortran dilinde bir kod yazılmıştır. Herhangi bir cismin yüzeyi grafik yazılımları kullanılarak herhangi büyüklükteki üçgen plakar halinde modellenmiştir. Üçgen plaka modeli verilen herhangi bir cismin Fiziksel Optik yüzey integrali tüm yüzey üzerinde hesaplanmıştır. Yüzeyin asıl şekli değişmedikçe, üçgen plakaların büyüklüğünde sınır yoktur.

Daha iyi sonuç elde etmek için gölgeleme algoritması kullanılmıştır. Fiziksel optik yansıma noktaları yüzey üzerinde görüntülenmiştir.

İndüklenmiş yüzey akımları ve radar kesit alanı basit cisimler için ve F-16 uçaklarının yakıt tankı için hesaplanmıştır. İndüklenmiş yüzey akımları cisimler üzerinde görüntülenmiştir.

Anahtar kelimeler: Fiziksel optik teorisi, fiziksel kırınım teorisi, radar kesit alanı, üçgen plakalarla modelleme, empedans yüzeyden saçınım.

ACKNOWLEDGMENTS

I gratefully thank my supervisor Prof. Dr. Ayhan Altıntaş for his suggestions, supervision, and guidance throughout the development of this thesis.

I would also like to thank Asst. Prof. Dr. Vakur B. Ertürk, and Prof. Gülbin Dural, the members of my jury, for reading and commenting on the thesis.

Additionally, I thank to Alev Kuruoglu and Erinç Albayrak for their help on checking the grammar and typing errors of this thesis.

Lastly, thanks to TUSAŞ AŞ for supplying the model of fuel tank of F-16 airplanes and supporting this work.

Contents

1 INTRODUCTION **1**

2 THEORY **5**

2.1 Physical Optics for Conducting Objects 6

2.1.1 Coordinate Transformations 8

2.1.2 Solution for Single Triangular Plate 11

2.1.3 Multiple Plates 15

2.2 Equivalent Edge Currents 16

2.2.1 Formulation 16

2.2.2 PTD-EEC Formulation 21

2.2.3 PTD-EEC for a Wedge 24

3 APPLICATIONS BY PO **28**

3.1 Basic Shapes 29

3.2 Application to Fuel Tank of F-16 Airplanes 33

3.2.1 Modeling and Triangulation 33

3.2.2 Induced Surface Currents 34

3.2.3 RCS Results 36

4 APPLICATIONS BY PTDEEC 47

4.1 Basic Shapes 47

4.2 Application to Fuel Tank 49

5 PO FOR IMPEDANCE SURFACES 53

5.1 Formulation 55

5.1.1 Solution for a Single Triangle 56

5.2 Applications and Comparisons 58

6 SHADOWING 63

6.1 Methodology 64

6.2 Ray Intersection Algorithm 65

6.3 Results 67

7 FLASH POINT ANALYSIS 70

7.1 Visualization of Surface Currents Due to Scattering and Diffraction 70

7.2 Square Plate 73

8 CONCLUSIONS 78

List of Figures

2.1 Local coordinates of a triangle residing in global coordinates . . . 9

2.2 The triangle in local coordinates 10

2.3 Illustration of scattering mechanism. 17

2.4 Integration variables dl, $\hat{u}$ and tangent vector $\hat{t}$. 19

2.5 Integration variables dl, $\hat{u}$ and tangent vector $\hat{t}$. 21

2.6 Wedge geometry. 26

3.1 Sphere divided into triangular meshes. 30

3.2 Backscattered RCS versus frequency of a sphere of radius 1m . . . 31

3.3 GO reflected and PO diffracted fields. 31

3.4 Backscattered RCS versus aspect angle of a sphere of radius 1m at 300MHz 32

3.5 Bistatic RCS versus aspect angle of a sphere of radius 1m at 300MHz, horizontal polarization 33

3.6 Bistatic RCS versus aspect angle of a sphere of radius 1m at 300MHz, horizontal polarization 34

3.7 Backscattered RCS versus aspect angle of a cylinder of height radius 5λ and diameter 1λ at 266MHz 35

3.8 Induced surface current on fuel tank, incidence angles $\theta = 45°$, $\phi = 0°$, vertical polarization 36

3.9 Induced surface current on fuel tank, incidence angles $\theta = 45°$, $\phi = 0°$, horizontal polarization 37

3.10 Induced surface current on fuel tank, incidence angles $\theta = 45°$, $\phi = 90°$, vertical polarization 38

3.11 Induced surface current on fuel tank, incidence angles $\theta = 45°$, $\phi = 90°$, horizontal polarization 39

3.12 Induced surface current on fuel tank, incidence angles $\theta = 45°$, $\phi = 160°$, vertical polarization 39

3.13 Induced surface current on fuel tank, incidence angles $\theta = 45°$, $\phi = 160°$, horizontal polarization 40

3.14 Imaginary part of induced surface current on fuel tank, incidence angles $\theta = 45°$, $\phi = 0°$, vertical polarization 40

3.15 Real part of induced surface current on fuel tank, incidence angles $\theta = 45°$, $\phi = 0°$, vertical polarization 41

3.16 Imaginary part of induced surface current on fuel tank, incidence angles $\theta = 45°$, $\phi = 90°$, vertical polarization 41

3.17 Real part of induced surface current on fuel tank, incidence angles $\theta = 45°$, $\phi = 90°$, vertical polarization 42

3.18 Imaginary part of induced surface current on fuel tank, incidence angles $\theta = 45°$, $\phi = 90°$, horizontal polarization 42

3.19 Real part of induced surface current on fuel tank, incidence angles $\theta = 45°$, $\phi = 90°$, horizontal polarization 43

3.20 Radar cross section of fuel tank, incidence angles $\theta = 45°$, frequency 1GHz. 43

3.21 Radar cross section of fuel tank, incidence angles $\theta = 45°$, frequency 20GHz. 44

3.22 Radar cross section of fuel tank, incidence angles $\theta = 45°$, frequency 13GHz(PO and GO solutions). 44

3.23 Radar cross section of fuel tank, incidence angles $\theta = 45°$, $\phi = 0°$. 45

3.24 Radar cross section of fuel tank, incidence angles $\theta = 45°$, $\phi = 90°$. 45

3.25 Radar cross section of fuel tank, incidence angles $\theta = 45°$, $\phi = 160°$. 46

4.1 Square plate configuration. 48

4.2 Square plate bistatic RCS versus aspect angle(vertical polarization) PO, PO+PTDEEC. 49

4.3 Square plate bistatic RCS versus aspect angle(vertical polarization) PTDEEC. 50

4.4 Bistatic RCS versus aspect angle(horizontal polarization) for a cylinder. MOM, PO, PO+PTDEEC. 51

4.5 Fuel tank RCS versus aspect angle(vertical polarization). 51

4.6 Fuel tank RCS versus aspect angle(horizontal polarization). 52

5.1 Bistatic scattering from a coated object. 54

5.2 Triangular impedance plate orientation. 56

5.3 RCS of a square sheet of 1m at 700MHz(Horizontal polarization). 59

5.4 RCS of a square sheet of 1m at 700MHz(Vertical polarization). . . 60

5.5 RCS of fuel tank at 13GHz($\theta = 45°$, Horizontal polarization). . . . 60

5.6 RCS of fuel tank at 13GHz($\theta = 45°$, Vertical polarization). 61

5.7 RCS of fuel tank at $\theta = 45°$, $\phi = 160°$ (Horizontal polarization). . 61

5.8 RCS of fuel tank at $\theta = 45°$, $\phi = 160°$ (Vertical polarization). . . . 62

6.1 Illustration of shadowing and shadowed triangles. 64

6.2 Triangle translation and change of the case of the ray origin. . . . 66

6.3 Two 1m square sheets on top of each other. 68

6.4 Two 1m square sheets on top of each other. 69

6.5 RCS of the fuel tank at 13GHz. 69

7.1 Eye function. 71

7.2 Fresnel zone and eye function illustration. 72

7.3 Model of visualization. 73

7.4 Flash point visualization of 300λ square plate for $\phi = 45°, \theta = 0°$. 74

7.5 Flash point visualization of 300λ square plate for $\phi = 45°, \theta = 45°$. 75

7.6 Flash point visualization of 300λ square plate for $\phi = 45°, \theta = 70°$. 76

7.7 Flash point visualization of sphere with radius of 1m for $\phi = 45°, \theta = 90°$. 76

7.8 Flash point visualization of sphere with radius of 1m for $\phi_i = \phi_s = 45°, \theta_i = 90°, \theta_s = 45°$. 77

8.1 Vertical polarization 81

8.2 Horizontal polarization 82

8.3 Mesh count versus performance of the program 83

To My Family . . .

Chapter 1

INTRODUCTION

When a perfectly conducting body is illuminated by an electromagnetic field, electric currents are induced on the surface of the body. These currents act as new sources and create an electromagnetic field radiated outward from the body. This field, called the scattered field, depends on the frequency and the polarization of the incident field. The scattered field is also related to the physical dimensions and shape of the illuminated body. According to the ratio between the wavelength of the incident field and the scattering body size, at least three scattering regimes can be defined. These are: Low-frequency scattering, resonant scattering and high frequency scattering. Radar Cross Section (RCS), which is the fictitious area of the target, characterizes the spatial distribution of the power of the scattered field.

In this thesis, RCS calculation of arbitrary shaped targets in high frequency regime is considered. Among high frequency scattering techniques, Physical Optics (PO) and Geometric Optics (GO) are the easiest to implement. GO is based on the classical ray-tracing of incident, reflected and transmitted rays. PO is based on the integration of induced currents predicted by GO.

According to GO, RCS is given by a very simple formula that involves the local radius of curvature at the specular point, even in bistatic directions. However, this simple prediction fails when radius of curvature becomes infinite. This is usually the case for flat surfaces. The PO surface integral approach in [1] gives the correct result around specular direction. However, PO may fail at wide angles from the specular direction. This failure can be eliminated by insertion of the effect of diffraction.

The phenomenon of diffraction was first introduced by Young, who described the source of this field as an interaction between all incremental elements of the edge. Young advocated that interaction of different edge elements with each other and with the GO field produces the observed interference pattern for the total field. The following are the well-known edge diffraction techniques: Keller's Geometrical Theory of Diffraction (GTD), Ufimtsev's Physical Theory of Diffraction (PTD) [2], [3]. Additionally, Uniform Geometrical Theory of Diffraction (UTD) of The Ohio State University and Uniform Asymptotic Theory (UAT) of University of Illinois are improved versions of Keller's GTD and described in [4] and [5]. Additionally, diffraction from corners can be included by corner diffraction coefficients formulated for GTD in [4]. Corner diffraction coefficients are based on heuristic modifications of the wedge or half-plane solutions. An emprical corner diffraction coefficient for PTD is reported by Hansen [6].

GO can be extended to include the edge or surface diffracted rays, leading to the Geometric Theory of Diffraction (GTD) developed by Keller. GTD is based on determining the fields due to stationary points on the edge and superposing the contributions of all stationary points. Scattered fields from other points are assumed to cancel each other. Diffracted field from a stationary point is simply calculated by the multiplication of the following four factors: The value of incident field at the scattering center, a diffraction coefficient, a divergence and a phase factor. The total field is found by superposing the diffracted and reflected field components.

GTD fails within the transition regions adjacent to the shadow boundaries. Uniform Geometrical Theory of Diffraction (UTD) and Uniform Asymptotic Theory (UAT) approaches overcome this failure of GTD. The GTD, UTD and UAT all generally fail in ray caustic regions. The method of Equivalent Edge Currents (EEC) is developed to overcome this failure. But this method does not address the singularities. Based on the EEC, Ufimtsev developed Physical Theory of Diffraction (PTD). PTD eliminates the singularities and approximates the edge contribution by subtracting the incident field and the PO field from the exact solution for the total field. As a result, PTD diffraction coefficients can be expressed as the difference of the GTD diffraction coefficients and a set of PO coefficients. Just like GTD being a correction to GO, the edge diffraction correction in the PO is obtained through the Physical Theory of Diffraction (PTD). Throughout this thesis, PO and PTD are studied to calculate total scattered field.

The scattering objects are modeled as triangular flat plates, and for each plate, the PO scattered field is computed. For RCS computations this plate-based PO is obtained analytically; giving rise to the simple and fast superposition of the fields from each plate. Therefore, the computational cost is independent of the size of the plates in the model. This approach is suitable for targets with flat surfaces.

A computer program is developed in Fortran for Radar Cross Section (RCS) calculations. The calculations are done for some simple shaped targets and solutions are compared with the ones currently available in the literature. The RCS of triangular flat plate model of the fuel tank of F-16 airplanes is also calculated as an example. The results are compared with the ray-tracing algorithm results based on GO. PTD correction is also applied to these targets.

Local property of high frequency phenomena can be shown by visualizing the PO surface currents. For this purpose, the flash points, mainly the dominant reflected and diffracted currents are visualized over the surface of a square plate.

PO is also applied to impenetrable objects modeled as impedance surface boundary conditions. A conducting body with material coating can be approximated as impedance sheet; under the assumption of thin coating with respect to the radius of curvature and free space wavelength. The surface of the targets also should be impenetrable. If the scattering object has an impedance surface, induced magnetic currents will be included in addition to the induced electric currents. Scattered field from an impedance surfaces is derived and results are tested for some targets.

Chapter 2

THEORY

Physical Optics is used for calculations of RCS of large targets having conducting surfaces. When a wave is incident on a body, surface current is induced over the enlighted regions. According to PO technique, scattering field is calculated by the integration of these surface currents over the surface of the target. For numerical evaluation of integrations, the surface of the target is divided into triangular plates. Scattered field from each triangle is calculated, afterwards, the total scattering field is found by summing up the contributions from each triangle.

Large targets are usually modeled by large number of triangles. PO integration on each of these triangles increases the computational complexity. If the surface of the target is flat, then the surface can be divided into larger triangular plates, as soon as the property(surface unit normal, surface impedance) of the surface does not change along the plate. Taking the PO integral over a large surface does not change the computational complexity, because samples must be taken during the integration, in order to account for the phase change over a single triangle. On the other hand, by analytical calculation of PO integral over the large triangular plates, the computation complexity can be significantly reduced and faster calculations can be achieved. The main idea of the analytical approach is, computing only a pre-calculated surface integral solution for a single triangle. Instead of taking an integral over the surface of the triangle, the solution of the integral is computed. The following sections provide the derivation of PO scattered field and the analytical calculation method.

2.1 Physical Optics for Conducting Objects

Physical Optics uses the following steps in order to find the scattered field.

1. The incident and reflected fields on the surface of the scatterer is found by Geometrical Optics. For an impenetrable scatterer, the sum of the incident and reflected fields is assumed to be the total field on the surface.

2. The current excited on the surface of the scatterer is found by the tangential components of the incident fields on the surface. Since the fields exist only on the illuminated portions of the scattering body, the PO current for a conducting body is given by;

$$\bar{J}_s = \begin{cases} 2\hat{n} \times \bar{H}^i & \text{,illuminated region,} \\ 0 & \text{,shadow region} \end{cases} \tag{2.1}$$

where $\hat{n}$ is the unit normal vector of the surface positioned outward and H^i is the magnetic field vector.

3. Using radiation integrals, PO surface current is integrated over the surface of the scatterer, to yield the scattered field.

4. The total PO field is given by the superposition of the incident and the scattered fields. That is;

$$\bar{E}^t = \bar{E}^i + \bar{E}^s \tag{2.2}$$

$$\bar{H}^t = \bar{H}^i + \bar{H}^s. \tag{2.3}$$

If the source illuminating the target is at a far enough distance, then the incident field can be taken as a plane wave. The incident electric and magnetic fields are given by the following expressions:

$$\bar{E}^i = \bar{E}_0^i e^{-jk_i\hat{k}_i\cdot\bar{r}} \tag{2.4}$$

$$\bar{H}^i = \bar{H}_0^i e^{-jk_i\hat{k}_i\cdot\bar{r}} \tag{2.5}$$

$$\bar{H}_0^i = \frac{1}{\eta}\hat{k}_i \times \bar{E}_0^i, \tag{2.6}$$

where $\bar{E}_0^i$ and $\bar{H}_0^i$ are real and constant amplitude vectors. η is the intrinsic impedance of free space, $\hat{k}_i$ is the propagation vector and in spherical coordinates it is given by

$$\hat{k}_i = -\left(\hat{x}sin\theta^i cos\phi^i + \hat{y}sin\theta^i sin\phi^i + \hat{z}cos\theta^i\right). \tag{2.7}$$

The incident electric field is written in terms of its orthogonal components as

$$\bar{E}^i = \left(E_\theta^i\hat{\theta}^i + E_\phi^i\hat{\phi}^i\right)e^{-jk\hat{r}_i\cdot\bar{r}}, \tag{2.8}$$

where (θ^i, ϕ^i) are the spherical coordinates of the source and $\left(\hat{r}^i, \hat{\theta}^i, \hat{\phi}^i\right)$ are the unit vectors. The incident magnetic field intensity is given by

$$\begin{aligned}\bar{H}^i &= \frac{1}{\eta}\hat{k}_i \times \bar{E}^i \\ &= \left(\bar{E}_\phi^i\hat{\theta}^i - \bar{E}_\theta^i\hat{\phi}^i\right)\frac{e^{-jk\hat{r}_i\cdot\bar{r}}}{\eta}.\end{aligned} \tag{2.9}$$

The vector potential of the scattered field at $\bar{r}_s$ is proportional to the surface integral of induced current and is given by

$$\bar{A}^s = \frac{\mu}{4\pi r_s}e^{-jkr_s}\int_S\int \bar{J}e^{jk\hat{r_s}\cdot\bar{r}}ds. \tag{2.10}$$

If the observation point is in the far-field, then the following approximation holds:

$$
\begin{aligned}
\bar{E}^s &= -jw\bar{A}^s, \\
&= -\frac{jw\mu}{2\pi r_s} e^{-jkr_s} \int_S\int \hat{n} \times \bar{H}^i e^{jk\hat{r_s}\cdot\bar{r}} ds. \qquad (2.11)
\end{aligned}
$$

Using equations (2.9) and (2.11) the scattered field is found by calculating the following integral equation:

$$
\bar{E}^s = \frac{e^{-jkr_s}}{r_s} \left(\bar{E}^i_\phi \hat{\theta}^i - \bar{E}^i_\theta \hat{\phi}^i \right) \times \left(\frac{j}{\lambda} \right) \int_S\int \hat{n} e^{jk(\hat{r_i}+\hat{r_s})\cdot\bar{r}} ds. \qquad (2.12)
$$

2.1.1 Coordinate Transformations

The scattered field from a conducting triangular plate will be computed using PO. The triangle is located arbitrarily in a global coordinate system. In order to have the equations less complicated, a local coordinate system can be defined. Let the triangle lie on the $x_l - y_l$ plane in the newly defined local coordinate system. If the edges of the triangle are called $\bar{e}_1$, $\bar{e}_2$ and $\bar{e}_3$, we can take $\bar{e}_3$ to be along y_l axis and one end of it at the origin of the local coordinate system (O_l). The local coordinates are found using the following equations:

$$
\hat{y}_l = -\frac{\bar{e}_3}{|\bar{e}_3|} \qquad (2.13)
$$

$$
\hat{z}_l = \frac{\bar{e}_1 \times (-\bar{e}_3)}{|\bar{e}_1 \times \bar{e}_3|} \qquad (2.14)
$$

$$
\hat{x}_l = \hat{y}_l \times \hat{z}_l \qquad (2.15)
$$

Fig. 2.1 depicts the triangle in the local and global coordinate systems. The vector $\bar{c}_l$ in Fig. 2.1 represents the distance between the global and local coordinate centers.

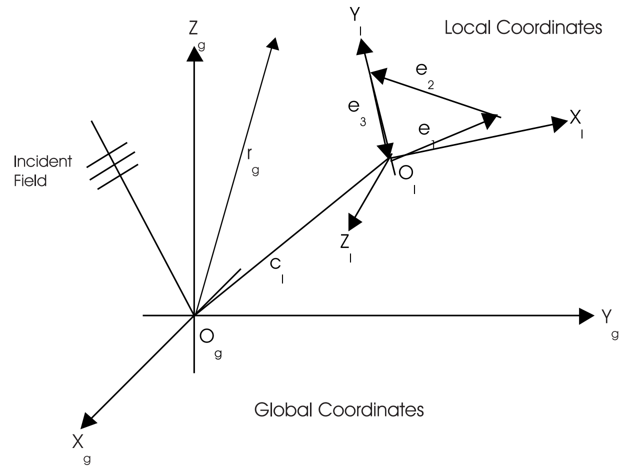

Figure 2.1: Local coordinates of a triangle residing in global coordinates

In order to find the PO scattered field from a triangle, PO field in the local coordinate system is calculated. Afterwards, it is transformed into global coordinates, where the total scattered field due to all of the triangles in the model is summed up.

The parametric expressions for edges $\bar{e}_1$ and $\bar{e}_2$ can be written in local coordinates as the following:

$$\alpha(x_l) = \alpha_0 + \alpha_1 x_l, \tag{2.16}$$

$$\beta(x_l) = \beta_0 + \beta_1 x_l. \tag{2.17}$$

Since $\bar{e}_1$ edge starts from the origin of the local coordinate system, α_0 should be equal to 0. The parameters in equations (2.16) and (2.17) are given as

$$\alpha_0 = 0, \tag{2.18}$$

$$\alpha_1 = \frac{e_{1y}}{e_{1x}}(e_{1x} \neq 0), \tag{2.19}$$

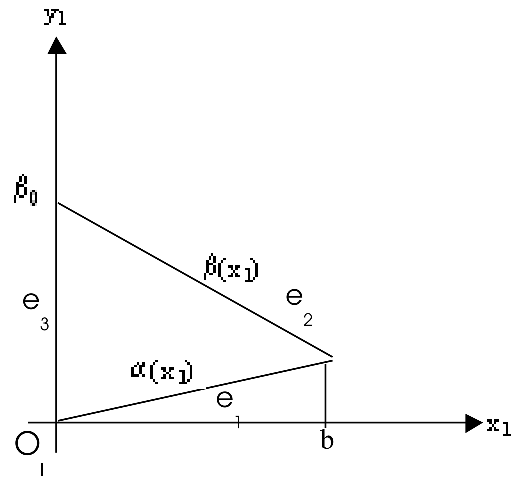

Figure 2.2: The triangle in local coordinates

$$\beta_0 = |\bar{e_3}|\,, \tag{2.20}$$

$$\beta_1 = -\frac{e_{2y}}{e_{2x}}. \tag{2.21}$$

The incident field given in the global rectangular coordinates should also be transformed into the local coordinate system. A transformation matrix $\bar{\bar{m}}_1$ is defined for transforming the incident field, propagating towards the origin of the global coordinate system, to the local rectangular coordinate system. So, the incident field in rectangular local coordinates is

$$(E^i_{xl}, E^i_{yl}, E^i_{zl}) = (E^i_{xg}, E^i_{yg}, E^i_{zg}) \cdot \bar{\bar{m}}_1, \tag{2.22}$$

where $\bar{\bar{m}}_1$ is;

$$\bar{\bar{m}}_1 = \begin{pmatrix} \hat{x_g} \cdot \hat{x_l} & \hat{x_g} \cdot \hat{y_l} & \hat{x_g} \cdot \hat{z_l} \\ \hat{y_g} \cdot \hat{x_l} & \hat{y_g} \cdot \hat{y_l} & \hat{y_g} \cdot \hat{z_l} \\ \hat{z_g} \cdot \hat{x_l} & \hat{z_g} \cdot \hat{y_l} & \hat{z_g} \cdot \hat{z_l} \end{pmatrix}. \tag{2.23}$$

Another matrix called $\bar{\bar{m}}_2$ is used to transform the incident field from the rectangular local coordinate system to the spherical local coordinate system, in which calculations for the scattered field will be done. The incident field in spherical local coordinates is found by

$$(E^i_{\theta l}, E^i_{\phi l}) = (E^i_{xl}, E^i_{yl}, E^i_{zl}) \cdot \bar{\bar{m}}_2, \tag{2.24}$$

where $\bar{\bar{m}}_2$ is;

$$\bar{\bar{m}}_2 = \begin{pmatrix} \hat{x}_l \cdot \hat{\theta}_l & \hat{x}_l \cdot \hat{\phi}_l \\ \hat{y}_l \cdot \hat{\theta}_l & \hat{y}_l \cdot \hat{\phi}_l \\ \hat{z}_l \cdot \hat{\theta}_l & \hat{z}_l \cdot \hat{\phi}_l \end{pmatrix}. \tag{2.25}$$

The matrix $\bar{\bar{m}}_2$ is found to be

$$\bar{\bar{m}}_2(\theta_l, \phi_l) = \begin{pmatrix} cos\theta_l cos\phi_l & -sin\phi_l \\ cos\theta_l cos\phi_l & cos\phi_l \\ -sin\theta_l & 0 \end{pmatrix}, \tag{2.26}$$

where θ_l and ϕ_l are the azimuth and elevation angles in local coordinates. In addition, in order to find the angle of incidence in local coordinates, θ^i_l and ϕ^i_l, the propagation vector is multiplied by $\bar{\bar{m}}_2$.

2.1.2 Solution for Single Triangular Plate

The incident field in rectangular local coordinate system (in its orthogonal components) is given by

$$\bar{E}^i_l(\bar{r}_l) = \left(E^i_{\theta l}\hat{\theta}^i_l + E^i_{\phi l}\hat{\phi}^i_l \right) e^{j\bar{k}_i \cdot \bar{r}_l}. \tag{2.27}$$

According to the Physical Optics method and as given in equation (2.1), the surface current induced on the +z side of the triangular plate is given as

$$\bar{J}_l^s(\bar{r}_l) = \frac{2e^{j\bar{k}_i\cdot\bar{r}_l}}{\eta}(\hat{x}_l(cos\phi_l^i E_{\theta l}^i - cos\theta_l^i sin\phi_l^i E_{\phi l}^i) + \hat{y}_l(sin\phi_l^i E_{\theta l}^i + cos\theta_l^i cos\phi_l^i E_{\phi l}^i)) \tag{2.28}$$

where $\bar{k^i} = k\hat{k^i}$, $\hat{k^i} = \hat{x}_l sin\theta_l^i cos\phi_l^i + \hat{y}_l sin\theta_l^i sin\phi_l^i + \hat{z}_l cos\theta_l^i$. k is the wave number, $\hat{k^i}$ is the unit vector along the direction of the incident wave, $\bar{r_l}$ is the position vector in local coordinates. The scattered field at some far zone observation point is written from the radiation integrals [7], as in [8];

$$E_{\theta l}^s(x_l, y_l) = \frac{-jw\mu}{4\pi r}e^{-jkr_i}\int_S\int(J_{xl}cos\theta cos\phi + J_{yl}cos\theta sin\phi - J_{zl}sin\theta)e^{jkg}ds', \tag{2.29}$$

$$E_{\phi l}^s(x_l, y_l) = \frac{-jw\mu}{4\pi r}e^{-jkr_i}\int_S\int(J_{xl}sin\phi + J_{yl}cos\phi)e^{jkg}ds', \tag{2.30}$$

where $g = x_l' sin\theta cos\phi + y_l' sin\theta sin\phi + z_l' cos\theta$. Integrals are calculated over the triangular planar surface, S. Distance r_l can be translated in the global coordinates as; $r_l = r_g - \hat{k_s}\cdot\bar{c_l}$. $\hat{k_s}$ is the unit vector in the direction of the propagation vector of the scattered field, $\bar{c_l}$ is the distance vector pointing the origin of the local coordinate system.

The equations (5.17) and (5.18) can be combined as a matrix equation:

$$\begin{bmatrix} E_\theta^s(r,\theta,\phi) \\ E_\phi^s(r,\theta,\phi) \end{bmatrix} = \bar{\bar{F}} \begin{bmatrix} E_\theta^s \\ E_\phi^s \end{bmatrix} \frac{2I_0}{\eta}\frac{jw\mu}{4\pi r}e^{-jkr}. \tag{2.31}$$

The components of the $\bar{\bar{F}}$ matrix are the following trigonometric expressions:

$$F_{11} = -cos\theta^s cos(\phi^s - \phi^i), \tag{2.32}$$

$$F_{12} = -cos\theta^s cos\theta^i sin(\phi^s - \phi^i), \tag{2.33}$$

$$F_{21} = sin(\phi^s - \phi^i), \tag{2.34}$$

$$F_{22} = -cos\theta^i cos(\phi^s - \phi^i). \tag{2.35}$$

The phase factor along the surface of the plate is taken into account by the integral I_0. The integral I_0 is given as

$$I_0 = \int_{x_l^{'}=a}^{b} \int_{y_l^{'}=\alpha(x_l^{'})}^{\beta(x_l^{'})} e^{j(ux_l^{'}+vy_l^{'})} dx_l^{'} dy_l^{'}, \tag{2.36}$$

where the terms u and v are

$$u = k(sin\theta^i cos\phi^i + sin\theta^s cos\phi^s), \tag{2.37}$$

$$v = k(sin\theta^i sin\phi^i + sin\theta^s sin\phi^s). \tag{2.38}$$

The limits of the integration are the edges of the particular triangle. The expressions for the integral limits are as follows:

$$\alpha(x_l^{'}) = \alpha_0 + \alpha_1 x_l^{'}, \tag{2.39}$$

$$\beta(x_l^{'}) = \beta_0 + \beta_1 x_l^{'}. \tag{2.40}$$

Using the above expressions, I_0 integral can be analytically calculated. The result is found to be

$$I_0 = \frac{1}{jv}(e^{jv\beta_0}\frac{e^{jb(u+v\beta_1)} - e^{ja(u+v\beta_1)}}{j(u+v\beta_1)} - e^{jv\alpha_0}\frac{e^{jb(u+v\alpha_1)} - e^{ja(u+v\alpha_1)}}{j(u+v\alpha_1)}). \tag{2.41}$$

Instead of computing the integral in 2.36, analytic solution in 2.41 is used. This approach yields faster computations.

It is noted that, for a triangle in local coordinates as in Fig. 2.2; a=0 and $\alpha_0 = 0$.

While computing equation (2.41), the expression scales down to simpler expressions for some limit cases.

If $u = v = 0$ then,

$$I_0 = (\beta_0 - \alpha_0)(b - a) + (\beta_1 - \alpha_1)\frac{b^2 - a^2}{2}. \quad (2.42)$$

If $u = 0$ then,

$$I_0 = \frac{1}{jv}(e^{jv\beta_0}\frac{e^{jbv\beta_1} - e^{jav\beta_1}}{jv\beta_1} - e^{jv\alpha_0}\frac{e^{jbv\alpha_1} - e^{jav\alpha_1}}{jv\alpha_1}). \quad (2.43)$$

If $v = 0$ then,

$$I_0 = (\beta_0 - \alpha_0)\frac{e^{jub} - e^{jua}}{ju} + (\beta_1 - \alpha_1)(\frac{be^{jub} - ae^{jua}}{ju} + \frac{1}{u^2}(e^{jub} - e^{jua})). \quad (2.44)$$

The scattered field from a single triangle in global coordinates can be defined in closed form as follows:

$$E^s(r_g, \theta_g, \phi_g) = C\bar{E}^i(0) \cdot \bar{\bar{m}}_1 \cdot \bar{\bar{m}}_2(\theta_l^i, \phi_l^i) \cdot \bar{\bar{F}} \cdot \bar{\bar{m}}_2^T(\theta_l^s, \phi_l^s) \cdot \bar{\bar{m}}_1^T \cdot \bar{\bar{m}}_2(\theta_g, \phi_g) \quad (2.45)$$

$E^s(r_g, \theta_g, \phi_g)$ represents the far-zone scattered field in the direction given by θ_g and ϕ_g in global coordinates. $E^i(0)$ includes the elements of the incident field in global coordinates. $\bar{\bar{m}}_1$ translates the incident field from global coordinates to the local coordinates. $\bar{\bar{m}}_2$ translates the cartesian coordinates to the spherical coordinates. The matrix $\bar{\bar{F}}$ is the Physical Optics scattering function in local coordinates defined in (2.31). $\bar{\bar{m}}_2^T$ converts the scattered field in local spherical coordinates to local cartesian coordinates. $\bar{\bar{m}}_1^T$ converts from the local coordinates to the global coordinates. Lastly, $\bar{\bar{m}}_2^T$ converts from global cartesian coordinates to global spherical coordinates. C is a complex number including the phase difference between local and global coordinate systems. In open form,

$$C = \frac{2I_0}{\eta}\frac{jw\mu}{4\pi r}e^{-jk(r-\hat{k_i}\cdot\bar{c_l}-\hat{k_s}\cdot\bar{c_l})} \tag{2.46}$$

Here $\bar{c_l}$ is the vector pointing the origin of the local coordinate system, $\hat{k}_i$ and $\hat{k}_s$ are the unit vectors showing the directions of the incident and scattered fields.

2.1.3 Multiple Plates

The scattered field solution from each illuminated triangle is summed up, in order to find the total scattered field. Afterwards, the well-known RCS formula in (2.47) and (2.48) are used to compute the RCS of the target for the horizontal and vertical polarizations respectively.

$$\sigma_{\theta\theta} = lim_{r\to\infty} 4\pi r^2 \frac{\left|\bar{E}^s_\theta\right|^2}{\left|\bar{E}^i_\theta\right|^2}, \tag{2.47}$$

$$\sigma_{\phi\phi} = lim_{r\to\infty} 4\pi r^2 \frac{\left|\bar{E}^s_\phi\right|^2}{\left|\bar{E}^i_\phi\right|^2}, \tag{2.48}$$

Radar Cross Section is a measure of power that is returned or scattered in a given direction and normalized with respect to the power density of the incident field. The scattered power should be normalized so that the decay due to spherical spreading of the scattered wave is eliminated. By multiplication factor $4\pi r$, RCS quantity is independent of the distance between the scatterer and the observation point. From the formula in (2.47) and (2.48), it is concluded that RCS is a function of target configuration, frequency, incident polarization and receiver polarization.

2.2 Equivalent Edge Currents

When a body is illuminated by a plane wave, current is induced on its surface. Around the edges of the body this current has more complicated behavior, due to the diffraction of the incident field. The edge diffracted field appears to come from a non-uniform line source located at the edge. So, the edge can be replaced by current sources along the edge. In the context of GTD, these currents are the GTD equivalent edge currents.

According to the method of equivalent edge currents; any finite current distribution yields a finite result for the far-zone diffracted field. By using proper current distribution on the edges, the invalidity of GTD diffraction at the caustics is avoided.

PO currents represent only the part of the exact induced current on the surface. This part is the uniform part. The rest is called the fringe or the non-uniform part and caused by the presence of the edges. The fields of fringe currents can be assumed to be caused by the equivalent edge currents located along the edge. This procedure of improving PO fields by the fringe fields of equivalent edge currents is called PTD. This approach was first introduced by Millar [10] and developed by Mitzner [11] and Michaeli [12]. The improved and modified equations for the equivalent edge currents in [13] is used throughout this work.

2.2.1 Formulation

In this section, scattering from flat plates is considered. Fig. 2.3 illustrates the scattering configuration. There are contributions from the surface of the plate and the edges of the plate. In order to calculate the equivalent edge currents along the edge of any flat plate with an arbitrary geometry, the edge is approximated with half planes. According the Physical Theory of Diffraction(PTD), the total scattered field is composed of two components; the Physical Optics(PO) field and the fringe wave(FW) field.

$$\bar{E}^s = \bar{E}^{PO} + \bar{E}^{FW}. \tag{2.49}$$

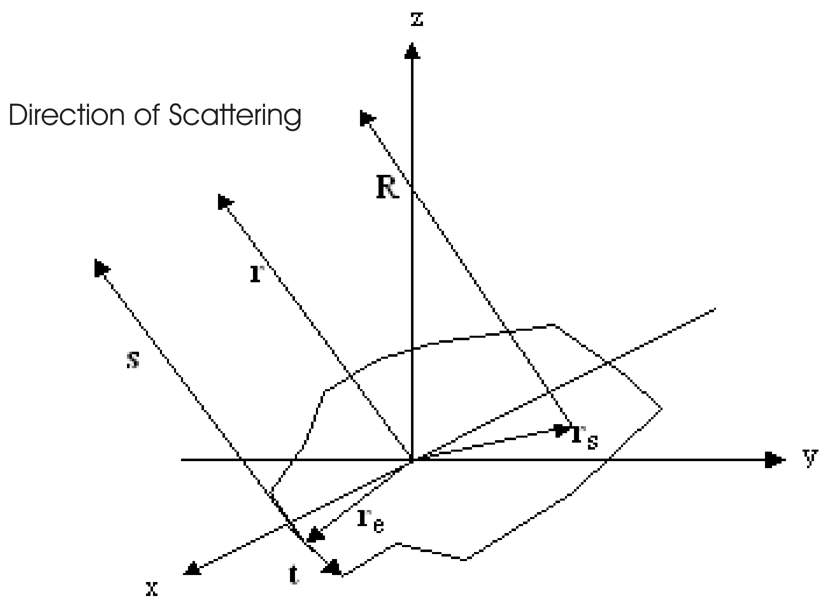

Figure 2.3: Illustration of scattering mechanism.

The two fields are caused by the physical optics and fringe wave surface current densities. The current induced over the surface of the scatterer can be decomposed into PO and non-uniform(fringe) components as in equation (2.50).

$$\bar{J}^{tot} = \bar{J}^{PO} + \bar{J}^{FW}. \tag{2.50}$$

These fringe wave field and fringe wave current are corrections to PO field and PO current; that is the exact solution of the total field is the sum of the PO contribution and the fringe wave contribution.

The first term in equation (2.49), that is the PO component has already been calculated. This chapter involves the calculation of the second term of equation (2.49).

For any far-field observation point, the scattered field due to the induced current on a surface S is given by

$$\bar{E}^s(r) = jk\eta \int\int_S \hat{R} \times (\hat{R} \times \bar{J}) \frac{e^{-jkR}}{4\pi R} ds'. \tag{2.51}$$

In order to calculate the fringe wave contribution to the total scattered field, the integral in equation (2.51) can be evaluated over the near-edge points, since the contribution from the rest of the surface is negligible. If this near-edge region is denoted as S_{edge}, then the total scattered field can asymptotically be expresses as follows:

$$\bar{E}^s(r) \approx \bar{E}_s^{PO} + jk\eta \int\int_{S_{edge}} \hat{R} \times (\hat{R} \times \bar{J}^{FW}) \frac{e^{-jkR}}{4\pi R} ds'. \tag{2.52}$$

Hence the scattered field due to fringe wave current, $\bar{J}^{FW}$, is given by

$$\bar{E}^{FW} \approx jk\eta \int\int_{S_{edge}} \hat{R} \times (\hat{R} \times \bar{J}^{FW}) \frac{e^{-jkR}}{4\pi R} ds'. \tag{2.53}$$

In order to compute the integral in equation (2.53), the integral is expressed in terms of new variables l and u, where l is the arc length along the edge and $\hat{u}$ is the unit vector perpendicular to the tangent of the edge, pointing inwards away from the edge. These variables are illustrated in Fig. 2.4.

For a far-field observation point, R in the phase term in equation (2.53) can be approximated as

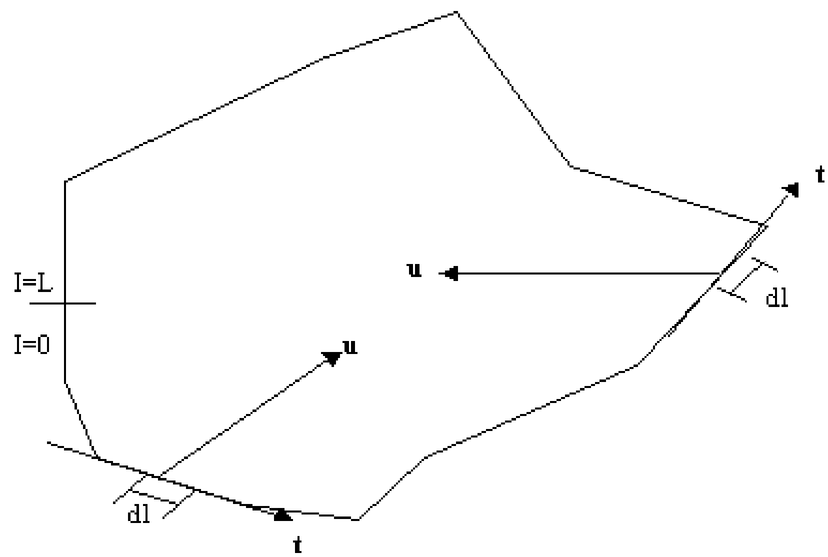

Figure 2.4: Integration variables dl, $\hat{u}$ and tangent vector $\hat{t}$.

$$R \approx s - \hat{s} \cdot (\bar{r}_s - \bar{r}_e) = s - \hat{s} \cdot \hat{u}u. \tag{2.54}$$

$\hat{R}$ in equation (2.53) can be approximated by $\hat{s}$ and the distance in denominator is approximated by s. Integration limits for the variable l is 0 and L, which is the total length of the edge. The variable u over the integration region is equal to 0. By the variable transformation the incremental area becomes

$$ds^{'} = \left|\hat{u} \times \hat{t}\right| dudl. \tag{2.55}$$

Using the above approximations and variable transformations, equation (2.53) is written as

$$\begin{aligned} \bar{E}^{FW} &\approx jk\eta \int\int_{S_{edge}} \hat{s} \times (\hat{s} \times \bar{J}^{FW}) \frac{e^{-jk(s-\hat{s}\dot{u}u)}}{4\pi s} ds^{'}, \\ &= jk\eta \int_0^L \int \left|\hat{u} \times \hat{t}\right| \frac{e^{-jk(s)}}{4\pi s} \times \left[\hat{s} \times \int_0 \bar{J}^{FW} e^{jk\hat{s}\dot{u}u} du\right] dl. \end{aligned} \tag{2.56}$$

The incremental diffracted field in (2.56) is the endpoint contribution, generated by J^{FW} on an incremental strip starting at the edge point and extending away from the edge in the direction of $\hat{u}$. This diffracted field is assumed to be generated by line currents on the edge. These electric and magnetic currents are located at the edges, at positions $\hat{r}_e$, and point at the same direction as the edge tangent vector $\hat{t}$. The diffracted field in terms of these edge currents can be written as

$$\bar{E} = jk \int_0^L \frac{e^{-jks}}{4\pi s} \left[\eta \hat{s} \times (\hat{s} \times \hat{t}) I^{FW} + \hat{s} \times \hat{t} M^{FW} \right] dl. \tag{2.57}$$

These electric and magnetic currents induced on the edges are expressed by equations (2.58).

$$\begin{aligned} I^{FW} &= \frac{\left|\hat{u} \times \hat{t}\right|}{\left|\hat{s} \times \hat{t}\right|^2} \hat{s} \cdot (\hat{t} \times \hat{s}) \times \int_0 \bar{J}^{FW} e^{jk\hat{s}\cdot\hat{u}u} du, \\ M^{FW} &= \eta \frac{\left|\hat{u} \times \hat{t}\right|}{\left|\hat{s} \times \hat{t}\right|^2} \hat{t} \cdot \hat{s} \times \int_0 \bar{J}^{FW} e^{jk\hat{s}\cdot\hat{u}u} du. \end{aligned} \tag{2.58}$$

The currents I^{FW} and M^{FW} given in equation (2.58) are called the Physical Theory of Diffraction Equivalent Edge Currents(PTDEEC). The term J^{FW} seen in equations (2.58) is the fringe wave surface current density and it is integrated along $\hat{u}$ to give the PTDEEC electric and magnetic currents. These PDTEEC currents are then integrated to give the fringe wave diffracted field, E^{FW}. PDTEEC is used as an improvement to PO for bodies having edges.

The actual edge is modeled as half planes, hence J^{FW} is the half plane current density and half plane current density is integrated along $\hat{u}$ in order to give I^{FW} and M^{FW}. The equivalent edge currents I^{FW} and M^{FW} depend on the tangential components of the incident electric and magnetic fields, the incidence and observation directions and the direction of $\hat{u}$.

2.2.2 PTD-EEC Formulation

Since the only contribution to the incremental diffracted field is from the edge, the result is equivalent, if the FW surface current is integrated from the edge extending to infinity. Therefore fringe wave parts of the equivalent edge currents in (2.58) are expressed as

$$
\begin{aligned}
I^{FW} &= \frac{\left|\hat{u} \times \hat{t}\right|}{\left|\hat{s} \times \hat{t}\right|^{2}} \hat{s} \cdot (\hat{t} \times \hat{s}) \times \int_{0}^{\infty} \bar{J}^{FW} e^{jk\hat{s}\cdot\hat{u}u} du, \\
M^{FW} &= \eta \frac{\left|\hat{u} \times \hat{t}\right|}{\left|\hat{s} \times \hat{t}\right|^{2}} \hat{t} \cdot \hat{s} \times \int_{0}^{\infty} \bar{J}^{FW} e^{jk\hat{s}\cdot\hat{u}u} du.
\end{aligned} \tag{2.59}
$$

The fringe wave component of the scattered field is found by applying the equations (2.59) to equation (2.56).

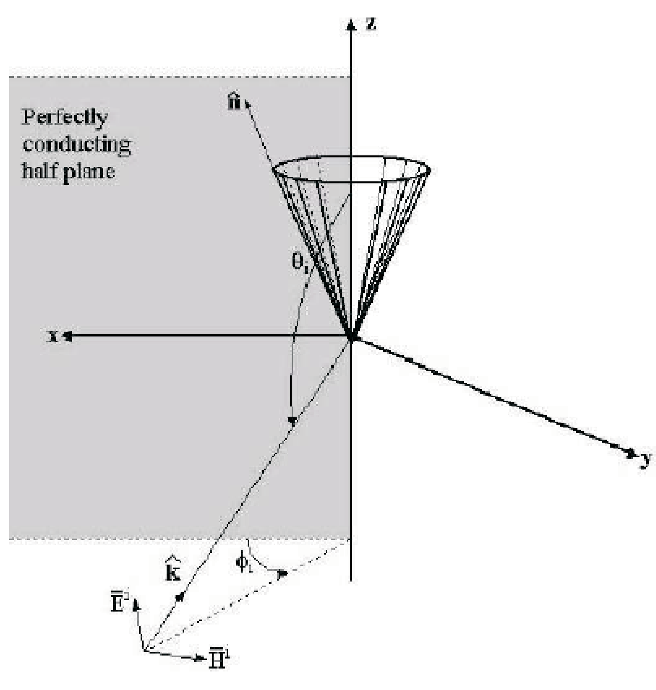

Figure 2.5: Integration variables dl, $\hat{u}$ and tangent vector $\hat{t}$.

Figure 2.5 illustrates the geometry of the problem of half plane illuminated by a plane wave. For this problem, the total field is found using the following boundary condition in cylindrical coordinates:

$$\bar{J}(\rho, z) = \hat{y} \times (\bar{H}(\rho, 0, z) - \bar{H}(\rho, 2\pi, z)). \tag{2.60}$$

The exact solution can be expressed as the following equations:

$$\begin{aligned}
E_z &= \bar{E}_0^i \cdot \hat{z}\frac{e^{j\pi/4}}{\sqrt{\pi}}[e^{jksin\theta^i\rho cos(\phi-\phi^i)}F(-\sqrt{2ksin\theta^i\rho}cos(\frac{\phi-\phi^i}{2})\\
&\quad -e^{jksin\theta^i\rho cos(\phi+\phi^i)}F(-\sqrt{2ksin\theta^i\rho}cos(\frac{\phi+\phi^i}{2}))]e^{jkzcos\theta^i},\\
H_z &= \bar{H}_0^i \cdot \hat{z}\frac{e^{j\pi/4}}{\sqrt{\pi}}[e^{jksin\theta^i\rho cos(\phi-\phi^i)}F(-\sqrt{2ksin\theta^i\rho}cos(\frac{\phi-\phi^i}{2})\\
&\quad -e^{jksin\theta^i\rho cos(\phi+\phi^i)}F(-\sqrt{2ksin\theta^i\rho}cos(\frac{\phi+\phi^i}{2}))]e^{jkzcos\theta^i},
\end{aligned} \tag{2.61}$$

where F is the Fresnel function given by

$$F(x) = \int_0^\infty e^{-jt^2}dt. \tag{2.62}$$

Using equations (2.62) and (2.61) with $\rho = x$, the FW surface current density is found to be

$$
\begin{aligned}
J_x^{FW}(x,z) &= -\bar{H}_0^i \cdot \hat{z} 4\frac{e^{j\pi/4}}{\sqrt{\pi}} F(\sqrt{2ksin\theta^i x}cos(\frac{\phi^i}{2})) \\
&\quad \cdot e^{jksin\theta^i cos(\phi^i)x + zcos\theta^i}, \\
J_z^{FW}(x,z) &= -(\frac{1}{\eta}\bar{E}_0^i \cdot \hat{z}\frac{sin\phi^i}{sin\theta^i} + \bar{H}_0^i \cdot \hat{z}\frac{cos\theta^i cos\phi^i}{sin\theta^i}) \\
&\quad \cdot 4\frac{e^{j\pi/4}}{\sqrt{\pi}} F(\sqrt{2kxsin\theta^i} cos\frac{\phi^i}{2}) e^{jk(xsin\theta^i cos\phi^i + zcos\theta^i)} \\
&\quad +(\frac{1}{\eta}\bar{E}_0^i \cdot \hat{z} sin\frac{\phi^i}{2} + \bar{H}_0^i \cdot \hat{z} cos\frac{\phi^i}{2} cos\theta^i) \\
&\quad \cdot 4\frac{-e^{j\pi/4}}{\sqrt{\pi}} \frac{1}{sin\theta^i \sqrt{2kxsin\theta^i}} e^{-jk(xsin\theta^i - zcos\theta^i)}.
\end{aligned} \tag{2.63}
$$

Since the integral variable u in equations (2.59) extend to infinity, it is required to have an asymptotic expression for the FW current. When the argument of Fresnel function is large enough, it can be approximated as

$$
lim_{x\to\infty} F(x) = \frac{e^{-jx^2}}{j2x}. \tag{2.64}
$$

Applying equation (2.64) to equations (2.65), the FW expressions reduces to

$$
\begin{aligned}
J_x^{FW}(x,z) &= -\bar{H}_0^i \cdot \hat{z}\frac{2e^{-j\pi/4}}{\sqrt{\phi}} \frac{e^{-jk(xsin\theta^i - zcos\theta^i)}}{\sqrt{2kxsin\theta^i} cos\frac{\phi^i}{2}}, \\
J_z^{FW}(x,z) &= -\bar{H}_0^i \cdot \hat{z}\frac{2e^{-j\pi/4}}{\sqrt{\phi}} \frac{cos\theta^i}{sin\theta^i} \frac{e^{-jk(xsin\theta^i - zcos\theta^i)}}{\sqrt{2kxsin\theta^i} cos\frac{\phi^i}{2}}.
\end{aligned} \tag{2.65}
$$

Total fringe wave can asymptotically be expressed as

$$
J^{FW}(x,z) = -\hat{u}\bar{H}_0^i \cdot \hat{z}\frac{2e^{-j\pi/4}}{\sqrt{\pi}} \frac{e^{-jk\hat{u}\cdot\bar{r}}}{\sqrt{2kxsin\theta^i} cos\frac{\phi^i}{2} sin\theta^i}, \tag{2.66}
$$

where

$$
\hat{u} = \hat{x}sin\theta^i - \hat{z}cos\theta^i. \tag{2.67}
$$

The equation (2.67) shows that the line that J^{FW} is integrated along, is the intersection of the Keller cone with the surface of the half plane in the same direction with $\hat{n}$. This is illustrated in Fig. 2.5.

2.2.3 PTD-EEC for a Wedge

The equations for computing the PTD-EEC for a wedge are developed by Michaeli [13]. The origin of the development of EEC equations is choosing the integral direction as the intersection of the Keller cone with the half plane surface. In order to apply the EEC method to a wedge, the problem of geometry is replaced with the one in 2.6. The equations for half plane directly apply to face 1. For face 2, x remains the same, y changes sign pointing the opposite direction and also z changes sign to $-z$. Using the change of variables in (2.68), EEC for face 2 can easily be calculated with the equations already derived for face 1.

$$z \rightarrow -z, \beta \rightarrow \pi - \beta, \beta^{'} \rightarrow \pi - \beta^{'}, \phi \rightarrow N\pi - \phi, \phi^{'} \rightarrow N\pi - \phi^{'}. \tag{2.68}$$

The total equivalent electric and magnetic currents take the form;

$$\bar{I} = (I_1 - I_2)\hat{z}, \tag{2.69}$$

$$\bar{M} = (M_1 - M_2)\hat{z}, \tag{2.70}$$

where $\bar{I}_1, \bar{M}_1$ are generated by the surface current density on face 1 and $\bar{I}_2, \bar{M}_2$ are generated by the surface current density on face 2. As mentioned before $\bar{I}_1, \bar{M}_1$ can be split into PO and FW components.

$$\bar{I}_1^f = I_1 - I_1^{PO}, \tag{2.71}$$

$$\bar{M}_1^f = M_1 - M_1^{PO}, \tag{2.72}$$

where from [13]

$$\begin{aligned} I_1^{PO} &= \frac{2jU(\pi-\phi')}{ksin\beta'(cos\phi'+\mu)}[\frac{sin\phi'}{Zsin\beta'}\hat{z}\cdot\bar{E}_0^i \\ &- (cot\beta' cos\phi' + cot\beta cos\phi)\hat{z}\cdot\bar{H}_0^i] \\ M_1^{PO} &= \frac{-2jZsin\phi U(\pi-\phi')}{ksin\beta sin\beta'(cos\phi'+\mu)}\hat{z}\cdot\bar{H}_0^i, \end{aligned} \tag{2.73}$$

$$\begin{aligned} I_1 &= \frac{2j}{ksin\beta'}\frac{1/N}{cos\frac{\phi'}{N} - cos\frac{\pi-\alpha}{N}}\cdot[\frac{sin\frac{\phi'}{N}}{Zsin\beta'}\hat{z}\cdot\bar{E}_0^i \\ &+ \frac{sin\frac{\pi-\alpha}{N}}{sin\alpha}\cdot(\mu cot\beta' - cot\beta cos\phi)\hat{z}\cdot\bar{H}_0^i] \\ &- \frac{2jcot\beta'}{kNsin\beta'}\hat{z}\cdot\bar{H}_0^i, \\ M_1 &= \frac{2jZsin\phi}{ksin\beta sin\beta'}\frac{\frac{1}{N}sin\frac{\pi-\alpha}{N}csc\alpha}{cos\frac{\pi-\alpha}{N} - cos\frac{\phi'}{N}}\cdot\bar{H}_0^i, \end{aligned} \tag{2.74}$$

where Z is the intrinsic impedance, $\bar{E}_0^i$ and $\bar{H}_0^i$ are the incident electric and magnetic field vectors at the point of diffraction and $U(x)$ is the unit step function. The variables α, β and γ are defined by the following relations:

$$\begin{aligned} \alpha &= arccos\mu = -jln(\mu + j\sqrt{1-\mu^2}), \\ \mu &= \frac{cos\gamma - cos^2\beta'}{sin^2\beta'} = 1 - 2\frac{sin^2\frac{\gamma}{2}}{sin^2\beta'}, \\ cos\gamma &= \hat{u}\cdot\hat{s} = sin\beta' sin\beta cos\phi + cos\beta' cos\beta. \end{aligned} \tag{2.75}$$

Edge currents on edge 1 are calculated using the formula stated in equations (2.71), (2.72), (2.73) and (2.74). Edge currents on edge 2 are also calculated using the same formula but with the proper change of variables given in equation (2.68). The total equivalent edge currents can be expressed as

$$
\begin{aligned}
I^f &= I_1^f - I_2^f, \\
M^f &= M_1^f - M_2^f. \qquad (2.76)
\end{aligned}
$$

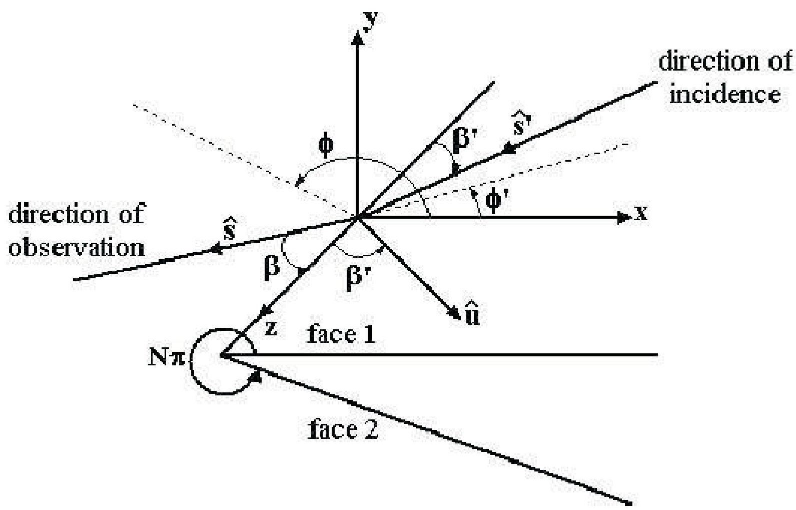

Figure 2.6: Wedge geometry.

Equations (2.77) are the final expressions for the equivalent edge currents for a half plane, where N=2 in Fig. 2.6.

$$
\begin{aligned}
I^f &= E_t^i \frac{2jY}{ksin^2\beta'} \frac{\sqrt{2}sin\frac{\phi'}{2}}{cos\phi' + \mu}[\sqrt{1-\mu} - \sqrt{2}sos\frac{\phi'}{2}] \\
&+ H_t^i \frac{2j}{ksin\beta'} \frac{1}{cos\phi' + \mu}[cot\beta' cos\phi' + cos\beta cos\phi \\
&+ \sqrt{2}cos\frac{\phi'}{2} \frac{\mu cot\beta' - cot\beta cos\phi}{\sqrt{1-\mu}}, \\
M^f &= H_t^i \frac{2jZsin\phi}{ksin\beta sin\beta'} \frac{1}{cos\phi' + \mu}[1 - \frac{\sqrt{2}cos\frac{\phi'}{2}}{\sqrt{1-\mu}}], \qquad (2.77)
\end{aligned}
$$

where $Y = Z^{-1}, E_t^i = \hat{z} \cdot \bar{E}_0^i, H_t^i = \hat{z} \cdot \bar{H}_0^i$.

In the case of half plane infinite singularity in edge currents for face 1 occurs when $\hat{s} = \hat{s}' = \hat{u}$ or $\beta = \beta', \phi' = \pi, \phi = 0$. A singularity for face 2 occurs when the observation direction is the continuation of a glancing incident ray coming from "outside" the wedge.

For the monostatic RCS calculations, the angles are $\beta = \pi - \beta^{'}, \phi = \phi^{'}$. The expression of α in equation (2.75) simplifies to the expressions given in (2.78) for faces 1 and 2.

$$\begin{aligned} \alpha_1 &= arccos\mu_1 = arccos(cos\phi - 2cot^2\beta), \\ \alpha_2 &= arccos\mu_2 = arccos(cos(N\pi - \phi) - 2cot^2\beta). \end{aligned} \tag{2.78}$$

Inserting the appropriate angles and α in (2.78) into (2.77), expressions in (2.79) and (2.80) are found for the backscattering case. The current densities for the backscattering case do not involve any singularities. Using these expressions, backscattered equivalent edge currents are computed.

$$\begin{aligned} I^f &= \frac{-2jY}{ksin^2\beta}[\frac{sin\phi U(\pi - \phi)}{cos\phi + \mu_1} + \frac{\frac{1}{N}sin\frac{\phi}{N}}{cos\frac{\pi-\alpha_1}{N} - cos\frac{\phi}{N}}]\hat{z} \cdot \bar{E}_0^i \\ &+ \frac{2jsin\frac{\pi-\alpha_1}{N}}{Nksin\beta sin\alpha_1}\frac{\mu_1 cot\beta^{'} - cot\beta cos\phi}{cos\frac{\phi}{N} - cos\frac{\pi-\alpha_1}{N}}\hat{z} \cdot \bar{H}_0^i \\ &-(\frac{-2jY}{ksin^2\beta}[\frac{sin(N\pi - \phi)U(\pi - N\pi + \phi)}{cos(N\pi - \phi) + \mu_2} \\ &+ \frac{\frac{1}{N}sin\frac{N\pi-\phi}{N}}{cos\frac{\pi-\alpha_2}{N} - cos\frac{N\pi-\phi}{N}}](-\hat{z} \cdot \bar{E}_0^i) \\ &\frac{2jsin\frac{\pi-\alpha_2}{N}}{Nksin\beta sin\alpha_2}\frac{cot\beta cos(N\pi - \phi) - \mu_2 cot\beta^{'}}{cos\frac{N\pi-\phi}{N} - cos\frac{\pi-\alpha_2}{N}}(-\hat{z} \cdot \bar{H}_0^i)). \end{aligned} \tag{2.79}$$

$$\begin{aligned} M^f &= \frac{2jZsin\phi}{ksin^2\beta}[\frac{sin\phi U(\pi - \phi)}{cos\phi + \mu_1} - \frac{\frac{1}{N}sin\frac{\pi-\alpha_1}{N}csc\alpha_1}{cos\frac{\phi}{N} - cos\frac{\pi-\alpha_1}{N}}]\hat{z} \cdot \bar{H}_0^i \\ &-(\frac{2jZsin(N\pi - \phi)}{ksin^2\beta}[\frac{U(\pi - N\pi + \phi)}{cos(N\pi - \phi) + \mu_2} \\ &- \frac{\frac{1}{N}sin\frac{\pi-\alpha_2}{N}csc\alpha_2}{cos\frac{N\pi-\phi}{N} - cos\frac{\pi-\alpha_2}{N}}])(-\hat{z} \cdot \bar{H}_0^i). \end{aligned} \tag{2.80}$$

Chapter 3

APPLICATIONS BY PO

For RCS computations, a computer program is written in Fortran. The program includes mesh generation algorithm for some simple shapes. The algorithm divides surfaces into triangular plates. External triangular plate models can also be exported into the program. These external triangular plate models can be generated using CAD tools like Autocad, IDEAS, etc. RCS of any target with the triangular mesh model given, can be calculated with the program.

For high frequency phenomena to be applicable, properties of the medium and the scatterer size should vary little over an interval on the order of a wavelength. Additionally, size of the scatterer must be large in terms of the wavelength at the given frequency. In order to comply with the criteria mentioned, targets having circular surfaces should be divided into smaller triangular plates. The mesh generation algorithm program assumes that maximum value of a triangular plate can be $\frac{\lambda^2}{200}$. Each triangular plate assumed to be equilateral triangles of edge length no more than $\frac{\lambda}{10}$, which is small enough for the high frequency approach. Smaller values give more accurate results causing an increase in the computational complexity.

The program has been used for calculation of RCS of some simple shapes. The results presented here conforms with the PO results in the literature [15]. This agreement does not mean that these results agree with the exact solution, but shows that computer program generates the correct PO data.

Additionally, RCS data is calculated for fuel tank of F-16 plane. The results are compared with the pre-computed ones using GO in [14].

This chapter represents the results for PO calculations only, whereas chapter 4 represents the PTDEEC results.

3.1 Basic Shapes

This section presents the numerical results of the Physical Optics formulation given in chapter 2 for some basic shapes, which have axial symmetry with respect to the z-axis. The radar cross section of a sphere with a radius of 1m is presented in Fig. 3.2. The model of the sphere consists of 25132 triangular plates and the size of each plate is 0,0005m^2. This value of mesh size is in accordance with $\frac{\lambda^2}{200}$ assumption around 1GHz. The mesh model is illustrated in Fig. 3.1. The plot in Fig. 3.2 depicts the backscattering RCS data versus frequency for axial incidence. The incidence and observation angles are $\theta = 0°$ and $\phi = 0°$.

In Fig. 3.2, it is observed that as the frequency increases, the RCS of the sphere approaches to πa^2, which is the exact result. πa^2 is the geometric cross section of the sphere, hence as the frequency increases, the PO solution approaches the Geometric Optics (GO) solution. The data is a good approximation to the exact solution in figure 6.4 in [9].

The oscillatory behavior of the solution is due to the interaction of GO reflected field contributions and the PO diffracted field contributions. The illustration of the PO and GO fields are shown in Fig. 3.3. GO reflected field

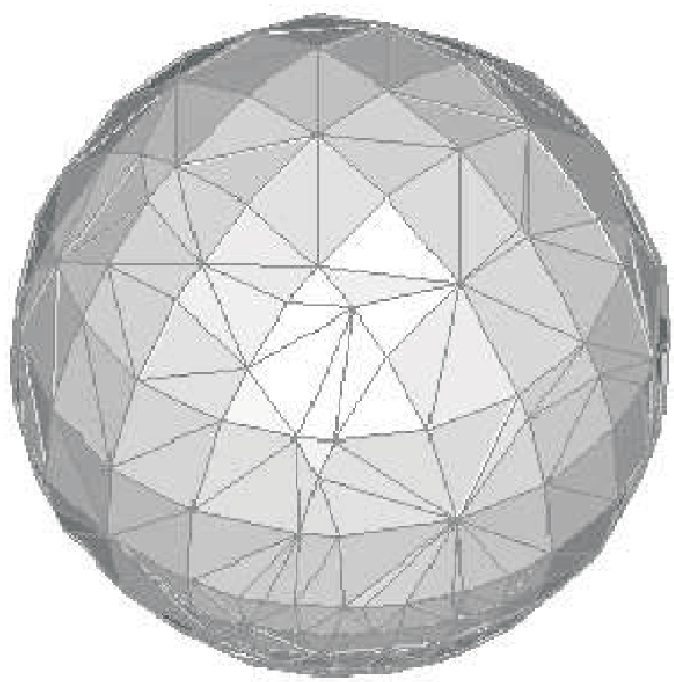

Figure 3.1: Sphere divided into triangular meshes.

corresponds to the stationary phase point contribution and the PO diffracted fields correspond to the end-point contribution in the asymptotic integration of PO. The PO diffracted field travels more than the GO reflected field does. The path difference, hence the phase difference between the PO and GO fields, is equal to the diameter (2m) of the sphere. Consequently, the peaks of RCS occur at every $\Delta f =$c/path difference ($\Delta f = 1.5 \cdot 10^8$), where c is the speed of light and it is equal to $3.10^8 m/s$.

The backscattered RCS solution of the sphere of radius 1m versus aspect angle is given in Fig. 3.4. Since the target is symmetric with respect to the origin, the RCS should be the same for every angle. However, the meshes generating the sphere does not sum up to have a perfectly smooth sphere surface, hence the RCS result is slightly varying around πa^2 rather than being constant. This result can be used to test whether the target is meshed adequately or not.

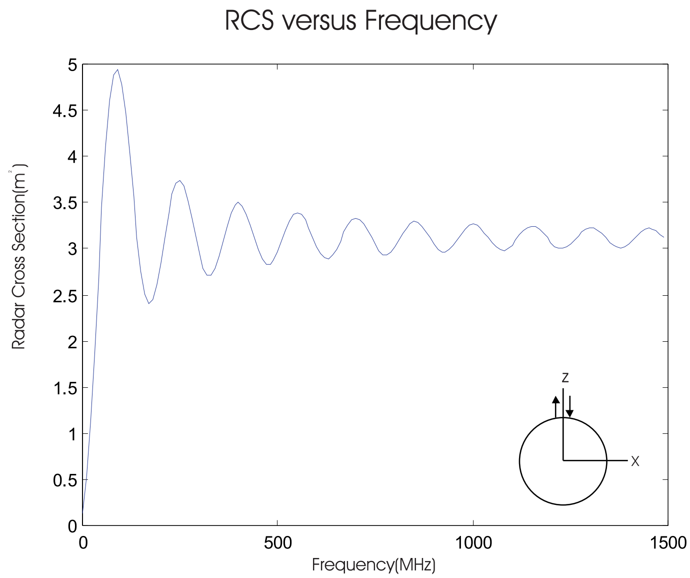

Figure 3.2: Backscattered RCS versus frequency of a sphere of radius 1m

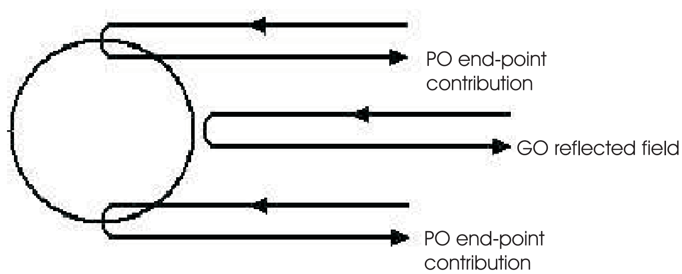

Figure 3.3: GO reflected and PO diffracted fields.

Figures 3.5 and 3.6 present the bistatic radar cross section data for the sphere of 1m for the cases in which the incident wave is horizontally and vertically polarized, respectively. The operating frequency is 300MHz. The source angles are ϕ=90 and $\theta = 0°$. The observation angle θ is changing from $0°$ to $180°$ and the observation angle ϕ is constant at $90°$. So, the incident and the scattered fields are on the same plane. It is observed that the RCS is largest at observation angle $\theta = 180°$. This is called the forward scattering direction.

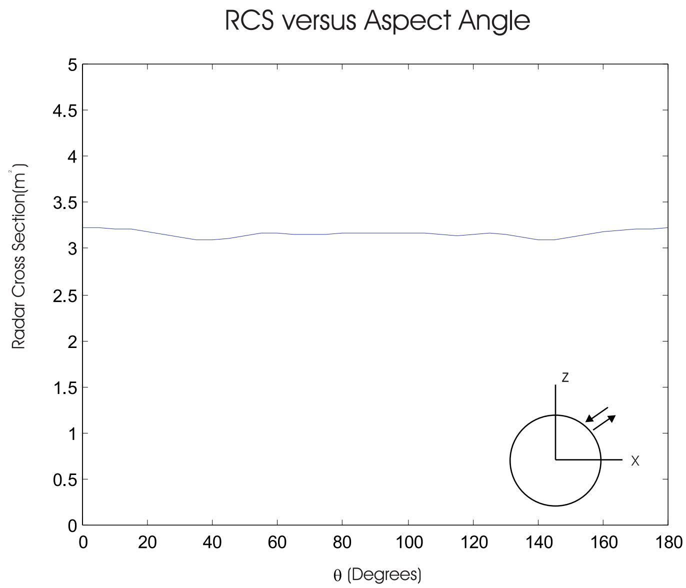

Figure 3.4: Backscattered RCS versus aspect angle of a sphere of radius 1m at 300MHz

The next basic shape is a cylinder of height 5λ and diameter 1λ. The number of meshes generating the cylinder is 95904. Fig. 3.7 shows the backscattered RCS data for this cylinder. The frequency is 266MHz. The elevation angle, ϕ, is constant and the azimuth angle, θ is rotated from 0 to 90°. The result is the same as the PO result given in [15]. The broadside RCS amounts to 20dBsm and the front face RCS to 9.9 dBsm.

The program computes the RCS of these basic shapes in a few seconds according to the selection of angle step. If the angle step is selected to be 5°, the computations took around 2 seconds. If the angle step is selected to be 1°, the computations took around 6 seconds.

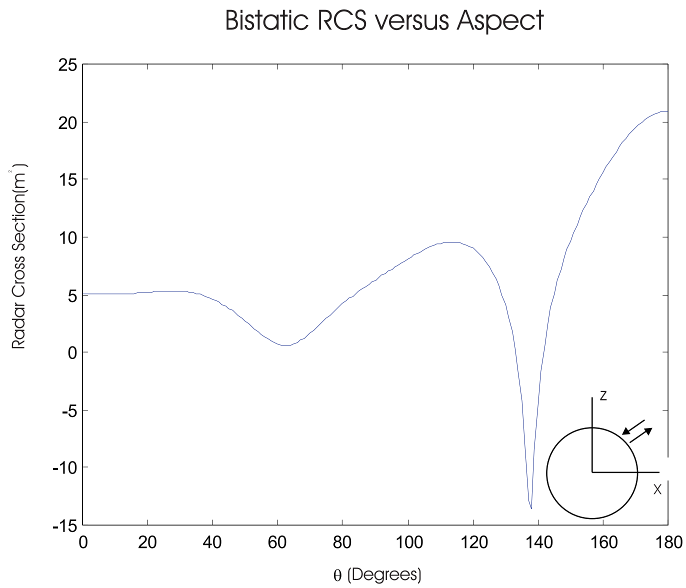

Figure 3.5: Bistatic RCS versus aspect angle of a sphere of radius 1m at 300MHz, horizontal polarization

3.2 Application to Fuel Tank of F-16 Airplanes

3.2.1 Modeling and Triangulation

The induced surface currents and RCS of Fuel Tank of F-16 airplane are studied as an other example. The triangular mesh model of fuel tank is supplied by Tusas A.S in ".raw" format. The total number of triangles generating the fuel tank is 136619. The model includes the coordinates of the triangles generating the fuel tank. The coordinates of triangles in the model are sequenced according to right hand rule. The normals of the triangles are calculated pointing outwards as required by the calculation program. The size of the fuel tank is approximately 5.5m in length and 0.66m in width. The fuel tank has two wings lying on x-axis, and the fuel tank itself is lying along z-axis. The fuel tank is thickest in the middle and it gets thinner towards its nose and there exist a concave tap at the back of the fuel tank.

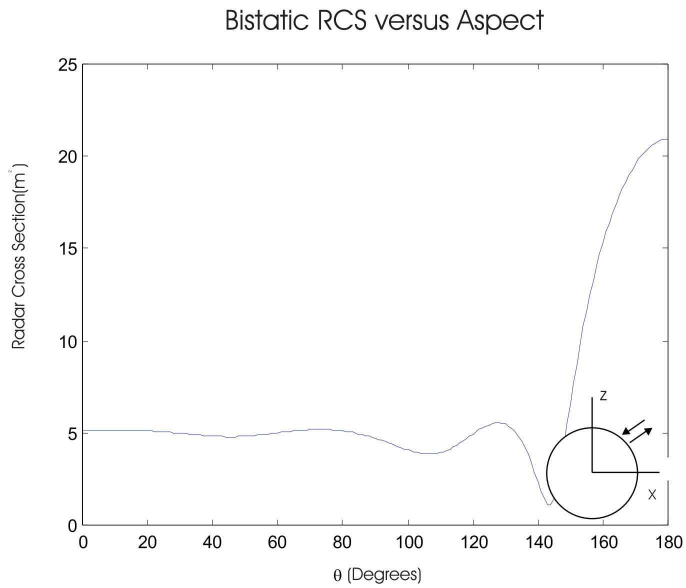

Figure 3.6: Bistatic RCS versus aspect angle of a sphere of radius 1m at 300MHz, horizontal polarization

3.2.2 Induced Surface Currents

The induced surface current is calculated using equation (2.28). The current can be calculated for any angle and polarization.

The visualization of induced currents is performed by Matlab. The colorbar on the right hand side of the fuel tank shows how the color change according to the current distribution, such that dark blue regions are in shadow and the red regions have the maximum current strength.

The horizontal and the vertical polarizations are defined according to the plane of incidence. When the electric field of incident wave is parallel to the plane of incidence, the polarization is called horizontal. When the E-field of incident wave is perpendicular to the plane of incidence, the polarization is called vertical. The polarizations for different incidence angles are illustrated in Fig. 8.1 and 8.2 in Appendix A.

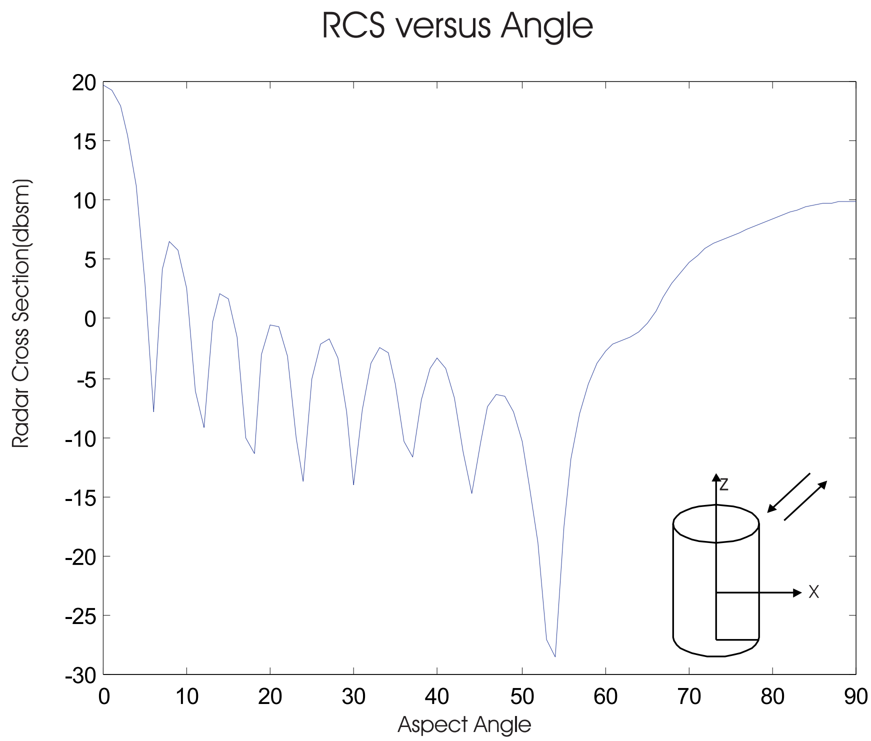

Figure 3.7: Backscattered RCS versus aspect angle of a cylinder of height radius 5λ and diameter 1λ at 266MHz

The Fig. 3.8, 3.9, 3.10, 3.11, 3.12, 3.13 show the induced surface current distribution for different angles and polarizations at 1GHz. Incidence angle is $\theta = 45°$ in all of the figures. It is observed that current distribution is maximum, where the surface normal is perpendicular to the H-field. The dark blue regions have no current, they are unilluminated by the incident field.

Due to the simplicity of the shape of the fuel tank, shadowing is not used for the calculation of induced surface current. Therefore, the regions around the wings, which are expected to be in shadow, do not seem to be shadowed. Instead the meshes in these regions have induced current as if they were not shadowed.

Fig. 3.14-3.19 show the real and imaginary parts of induced surface current. It is observed that real and imaginary parts are dominant at complementary

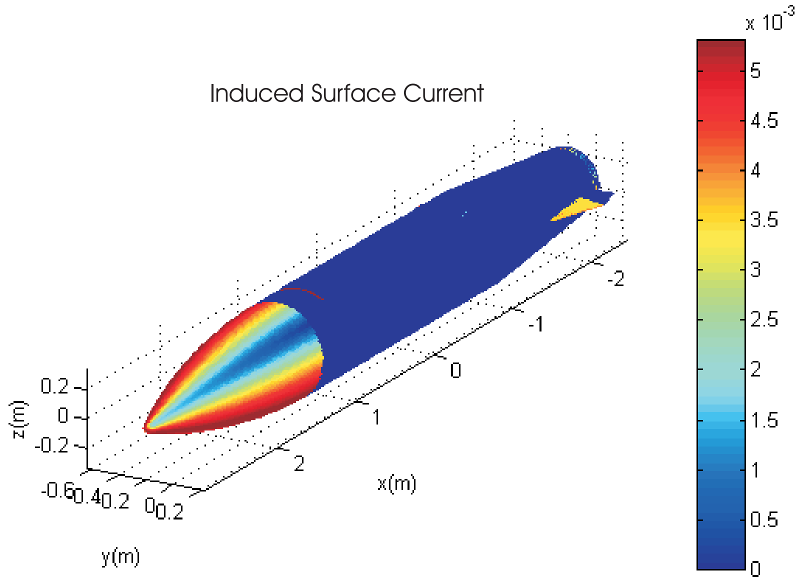

Figure 3.8: Induced surface current on fuel tank, incidence angles $\theta = 45°$, $\phi = 0°$, vertical polarization

regions and have a homogeneous current distribution in total, which was shown in Fig. 3.8-3.13.

3.2.3 RCS Results

Radar cross section of the fuel tank is calculated for any frequency and angle. During the calculation of radar cross section, shadowing is not used. Since the shape of the fuel tank is quite simple, the regions around the wings are expected to be in shadow, but this effect is neglected for the calculations.

Fig. 3.20, 3.21, 3.22 present the monostatic RCS data versus angle ϕ at different frequencies. Fig. 3.23, 3.24, 3.25 present the monostatic RCS data versus frequency at different angles, ϕ. Incidence angle θ is 45° for every plot. The RCS is given in dB over square meters. Since Physical Optics is polarization independent for monostatic RCS calculations, the RCS data for horizontal and vertical

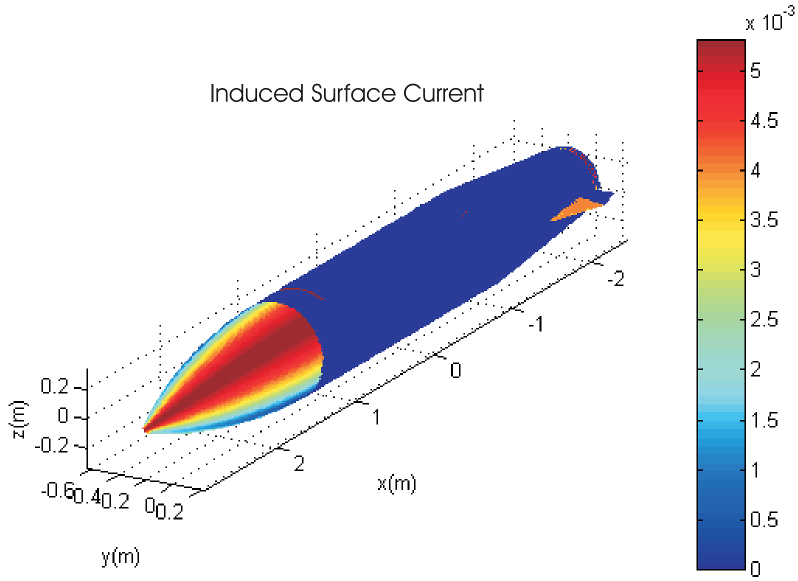

Figure 3.9: Induced surface current on fuel tank, incidence angles $\theta = 45°$, $\phi = 0°$, horizontal polarization

polarizations are the same. Hence the plots are valid for both polarizations. The plots show that the RCS for the fuel tank is maximum at $\phi = 90°$, where incident field is towards the middle of the fuel tank. This result is expected, because reflection is maximum at this angle. Additionally, the result at $\phi = 180°$(back of the fuel tank) is higher than the result at $\phi = 0°$. The reason for this result is that there exists a slightly spherical tap at the back of the fuel tank, whereas the nose has a very little smooth plane. Hence reflection back to the scattering direction is more powerful for the back of the fuel tank.

Fig. 3.22 shows the RCS data for both PO and GO solutions. The operating frequency is 13GHz. The plot with dashed line includes the results obtained using GO technique by Dr. A. Arif Ergin from Gebze Yüksek Teknoloji Enstitüsü. It is observed that PO solution is in accordance with the GO solution. The solution of GO includes both polarizations, whereas PO is polarization independent as

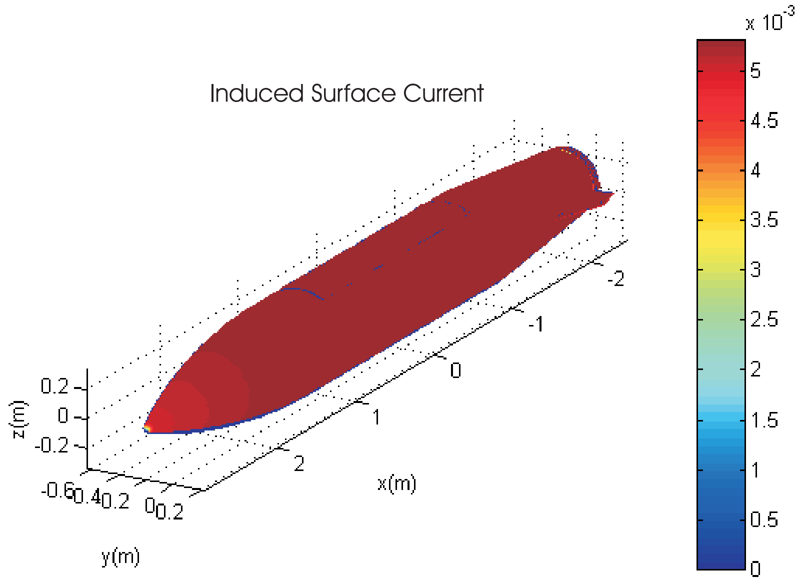

Figure 3.10: Induced surface current on fuel tank, incidence angles $\theta = 45°$, $\phi = 90°$, vertical polarization

mentioned before. The difference in the solutions are due to the fact that GO solution includes the multireflection effect, whereas PO solution does not.

The program computes the RCS of the fuel tank in approximately 10 seconds, when the angle step is selected as 10°. Since the model of the fuel tank includes over 139000 triangles, this calculation time can be considered pretty fast. Mesh count versus performance table of the program is depicted in Figure 8.3 in Appendix A.

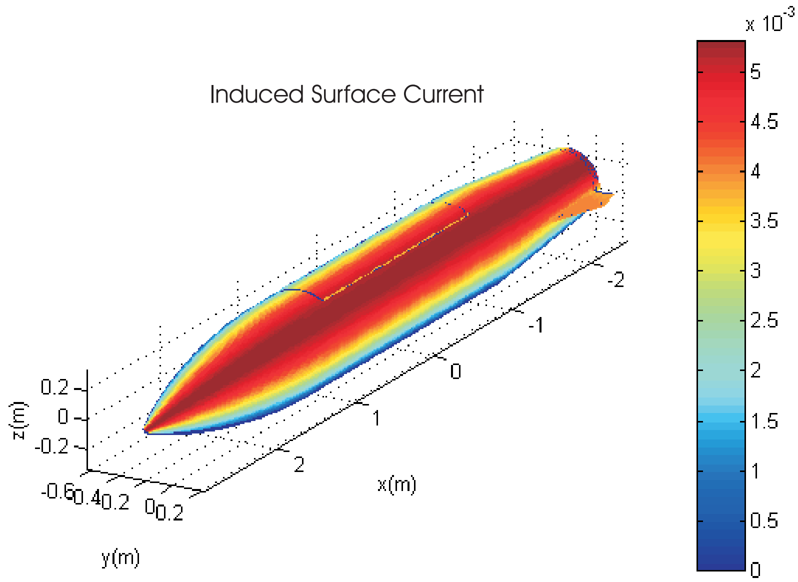

Figure 3.11: Induced surface current on fuel tank, incidence angles $\theta = 45°$, $\phi = 90°$, horizontal polarization

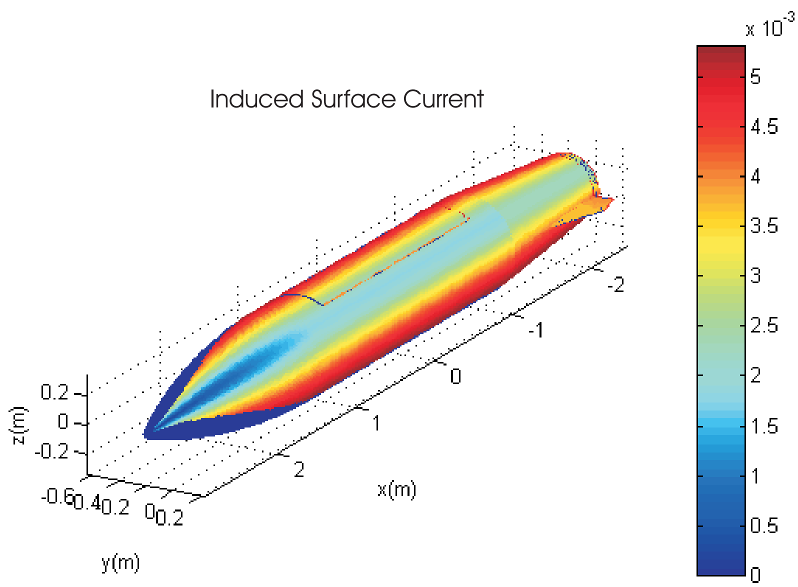

Figure 3.12: Induced surface current on fuel tank, incidence angles $\theta = 45°$, $\phi = 160°$, vertical polarization

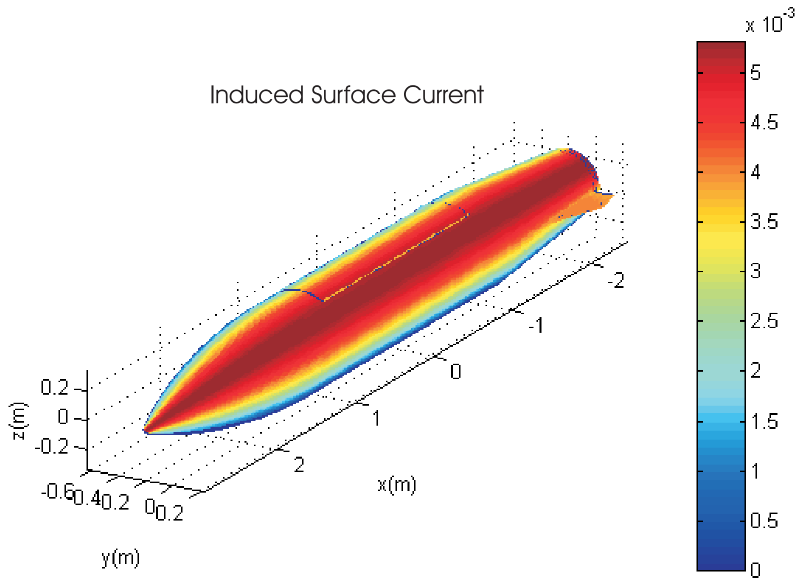

Figure 3.13: Induced surface current on fuel tank, incidence angles $\theta = 45°$, $\phi = 160°$, horizontal polarization

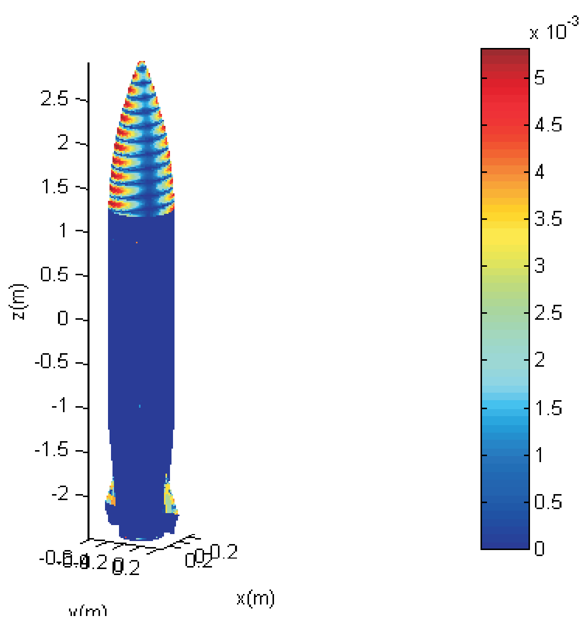

Figure 3.14: Imaginary part of induced surface current on fuel tank, incidence angles $\theta = 45°$, $\phi = 0°$, vertical polarization

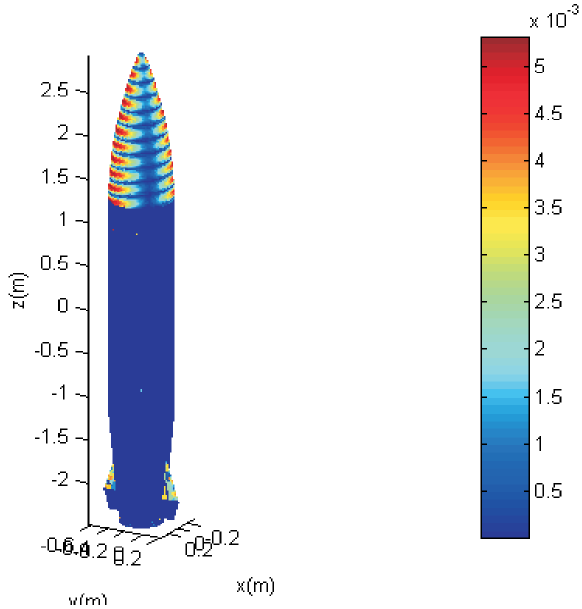

Figure 3.15: Real part of induced surface current on fuel tank, incidence angles $\theta = 45°$, $\phi = 0°$, vertical polarization

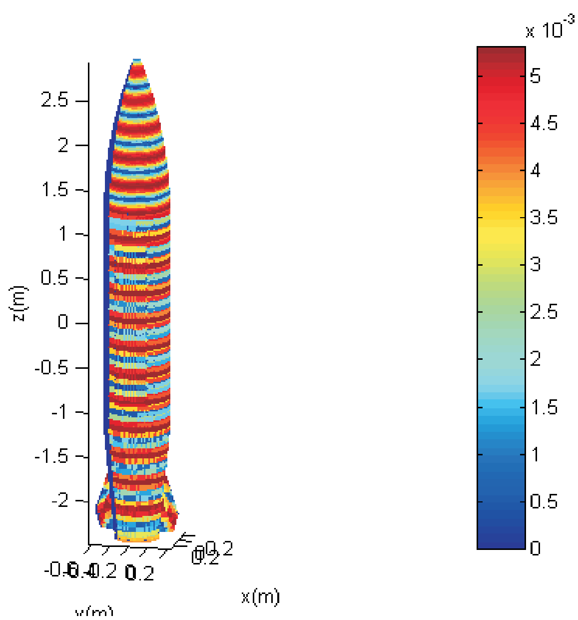

Figure 3.16: Imaginary part of induced surface current on fuel tank, incidence angles $\theta = 45°$, $\phi = 90°$, vertical polarization

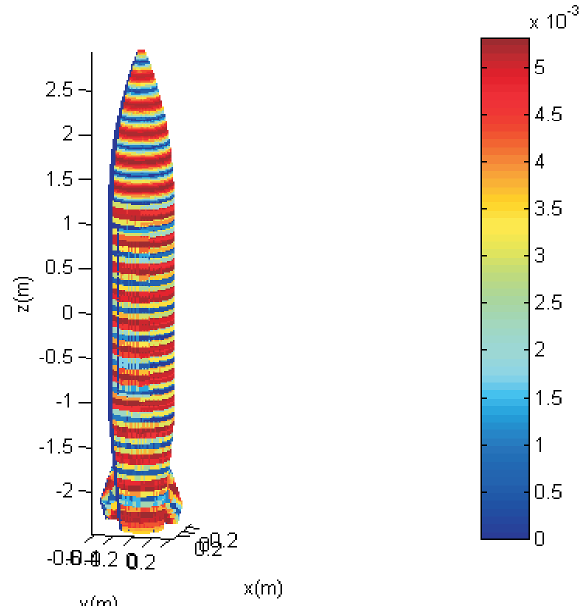

Figure 3.17: Real part of induced surface current on fuel tank, incidence angles $\theta = 45°$, $\phi = 90°$, vertical polarization

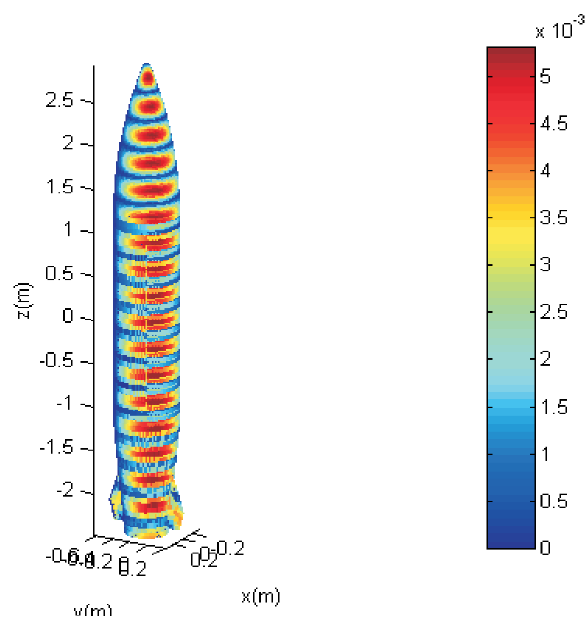

Figure 3.18: Imaginary part of induced surface current on fuel tank, incidence angles $\theta = 45°$, $\phi = 90°$, horizontal polarization

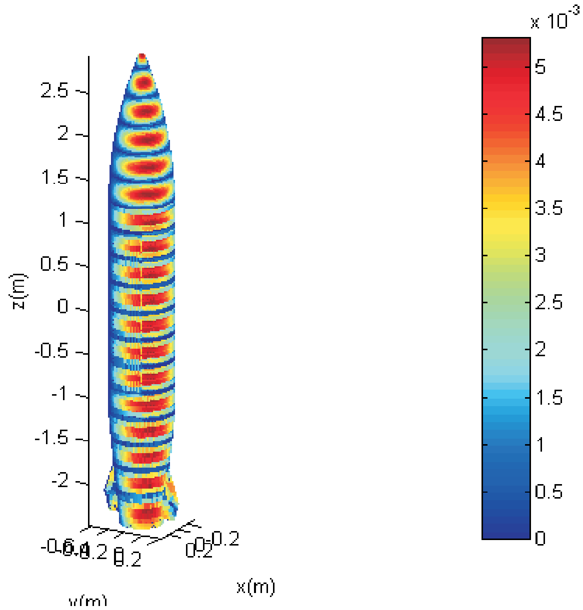

Figure 3.19: Real part of induced surface current on fuel tank, incidence angles $\theta = 45°$, $\phi = 90°$, horizontal polarization

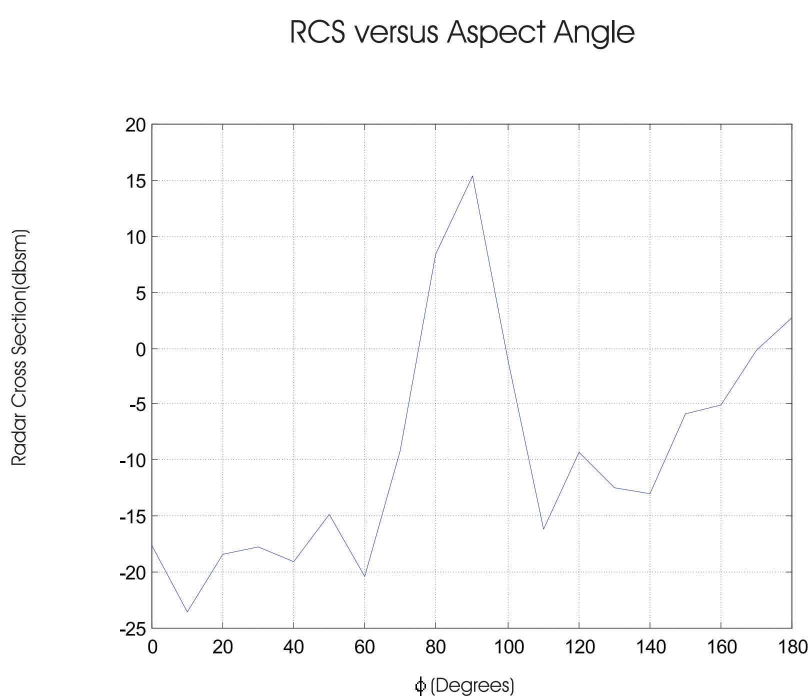

Figure 3.20: Radar cross section of fuel tank, incidence angles $\theta = 45°$, frequency 1GHz.

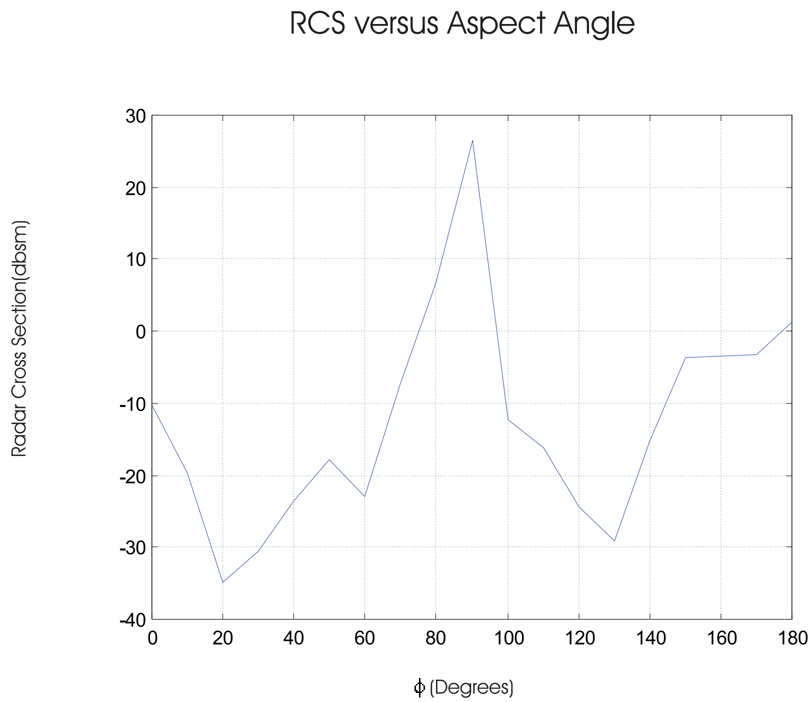

Figure 3.21: Radar cross section of fuel tank, incidence angles $\theta = 45°$, frequency 20GHz.

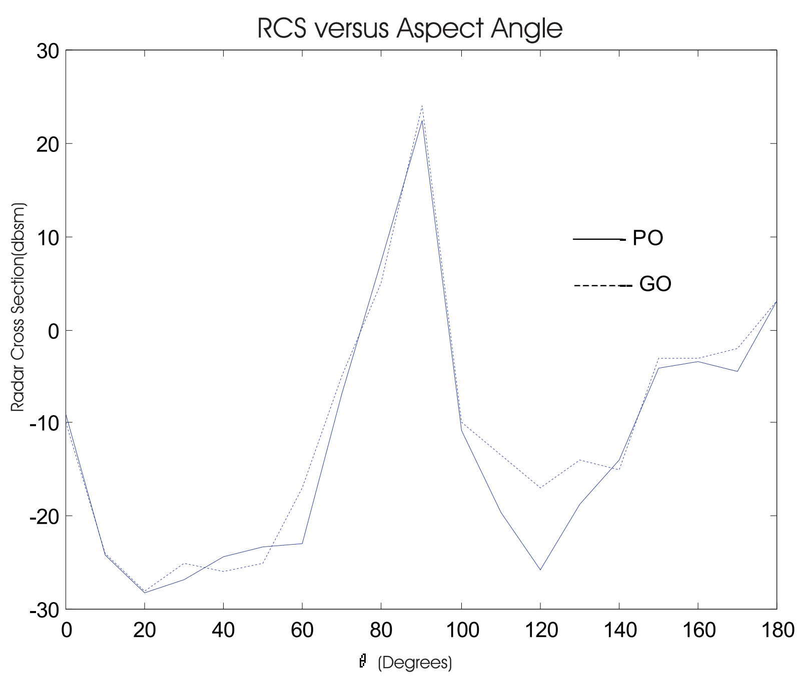

Figure 3.22: Radar cross section of fuel tank, incidence angles $\theta = 45°$, frequency 13GHz(PO and GO solutions).

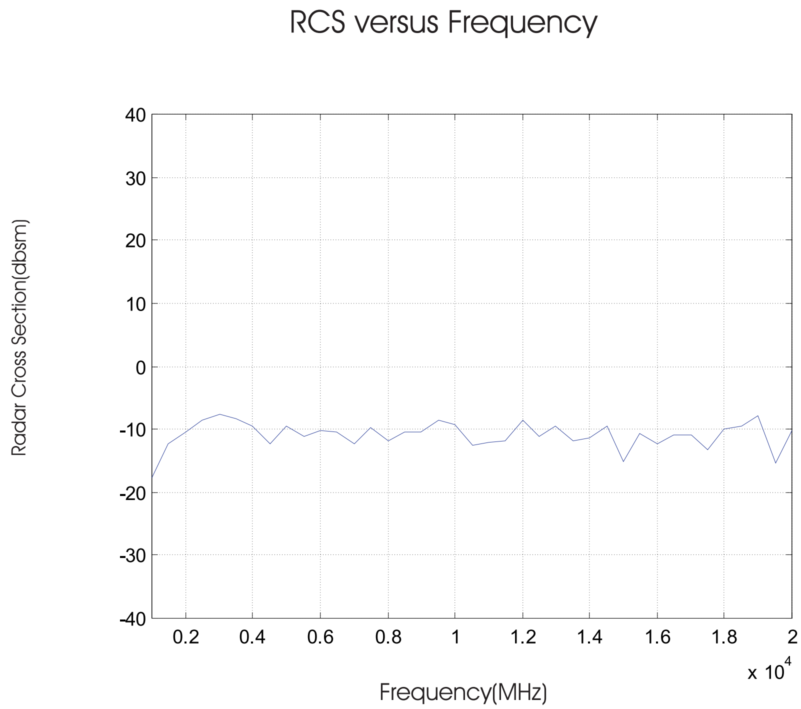

Figure 3.23: Radar cross section of fuel tank, incidence angles $\theta = 45°$, $\phi = 0°$.

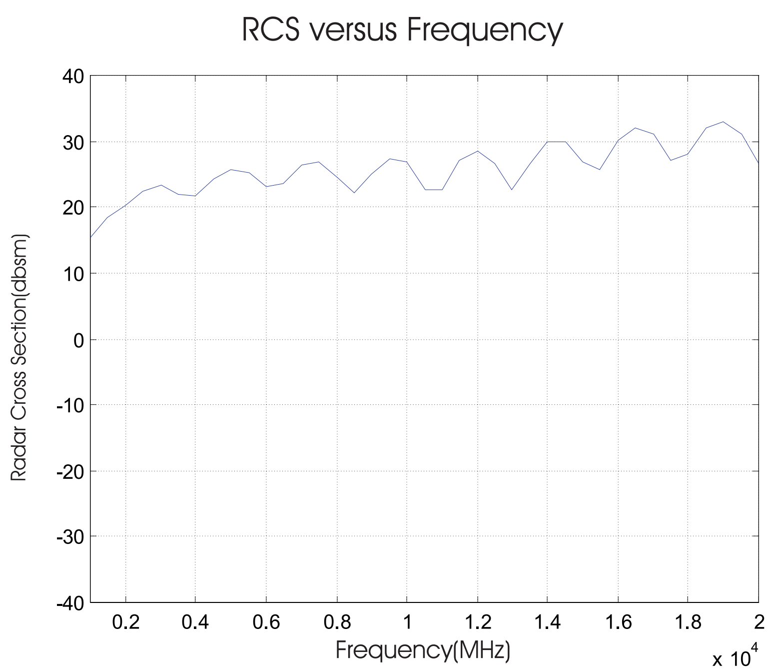

Figure 3.24: Radar cross section of fuel tank, incidence angles $\theta = 45°$, $\phi = 90°$.

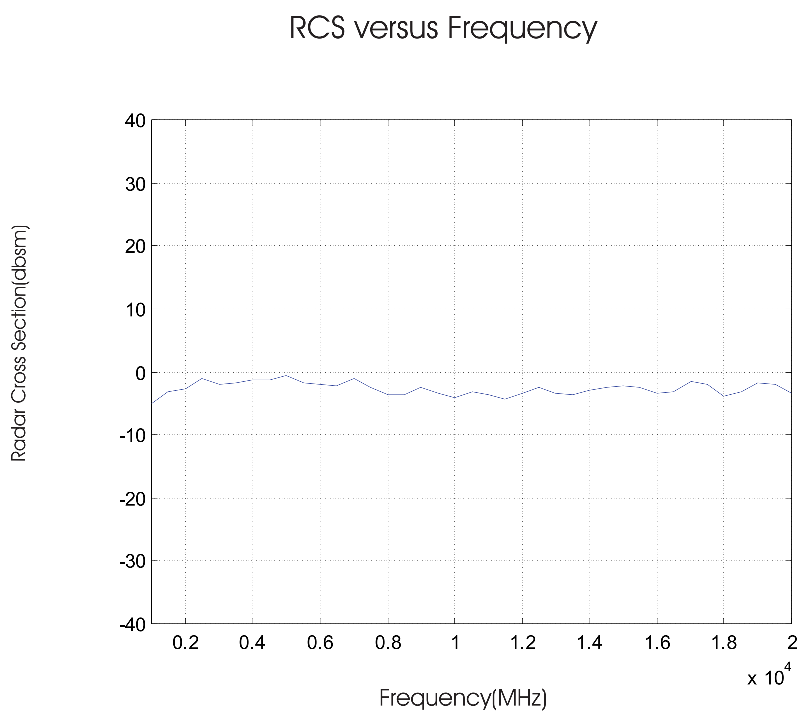

Figure 3.25: Radar cross section of fuel tank, incidence angles $\theta = 45°$, $\phi = 160°$.

Chapter 4

APPLICATIONS BY PTDEEC

Scattering data for the square plate is computed using PO and PTDEEC. RCS data of a cylinder is also calculated and the results are compared with the results available in the literature. Additionally, the scattering data involving the diffraction effect is computed for fuel tank model.

4.1 Basic Shapes

The square plate is illustrated in Fig. 4.1. The square plate is divided into 200 triangular plates. The area of each plate is equal to 0,005m^2. The equivalent edge currents I^f and M^f are calculated using expressions (2.77) with $\beta' = \phi' = \frac{\pi}{2}$ and $N = 2$. The RCS computations for this square plate took just a few seconds.

Fig. 4.2 depicts the bistatic RCS data of a square of 1 m, with respect to the aspect angle. The plot with the smooth line represents the PO, and the dashed line represents the sum of PO and PTDEEC results. The operating frequency is 1.8GHz and the incidence angles are $\theta^i = 0°$ and $\phi^i = 45°$. The observation angle is $\phi = 45°$. The polarization of the incident wave is vertical. It is observed that PTDEEC is more effective around 90 degrees. Since reflection is small

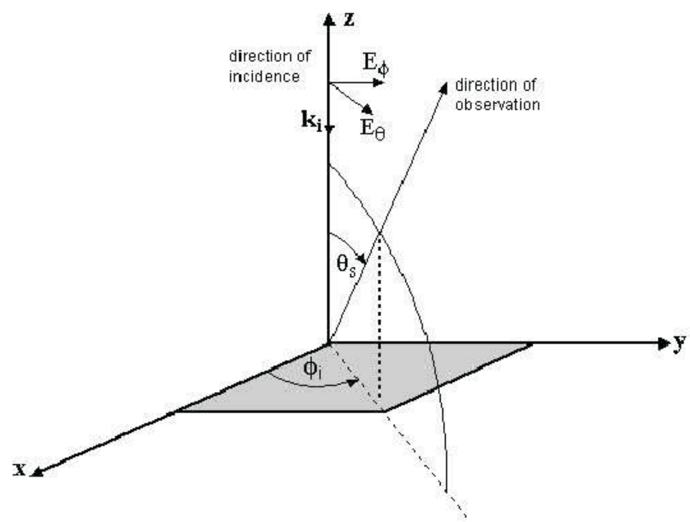

Figure 4.1: Square plate configuration.

around these angles, diffraction is more effective. Furthermore PTDEEC adds oscillations to the RCS result.

Fig. 4.3 represent only the PTDEEC component for the same configuration as in Fig. 4.2. It is observed that PTDEEC result has deep nulls throughout the pattern. This is due to the destructive interference of the fields caused by two orthogonal edges. Only the first order diffraction is considered in this work. Since the FW current is assumed to be travelling to infinity in accordance with the half plane geometry, diffraction caused by the same current at another edge is neglected. This second order diffraction effect is expected to be smaller for a larger plate.

The next basic shape is a cylinder with length $l = 1.98\lambda$ and base radius $a = 0.344\lambda$. The configuration of the cylinder and the backscattered RCS data are depicted in Fig. 4.4. The operating frequency is 2.6GHz and the polarization is horizontal. The Fig. 4.4 includes the RCS data by PO only, PO+PTDEEC

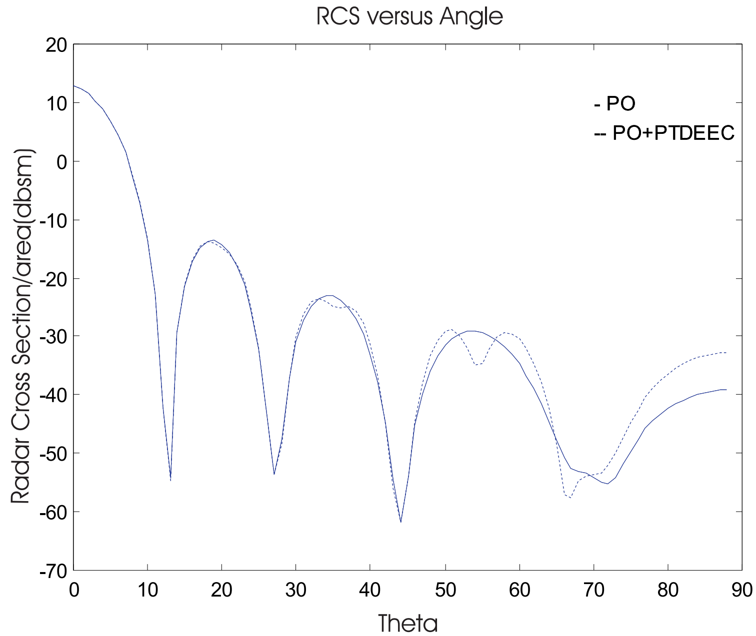

Figure 4.2: Square plate bistatic RCS versus aspect angle(vertical polarization) PO, PO+PTDEEC.

and experimental results from Shaeffer [16]. It is observed that addition of PTDEEC improves the PO only result, such that the total RCS data approaches to the experimental result. It should also be noted that not whole of the edge contributes to the PTDEEC. Because part of the edge may not be illuminated for some incidence angles.

4.2 Application to Fuel Tank

Fig. 4.5 and 4.6 show the backscattered RCS data for fuel tank for vertical and horizontal polarizations respectively. The operating frequency is 13GHz and the operating angle is $\phi = 45°$. The plot with the smooth line represent the PO and the dashed line represent the sum of PO and PTDEEC results. It is observed that the PTDEEC changes the RCS result mostly around $0°$ and $90°$. Around these angles reflection is less effective, hence diffraction dominates. Diffraction

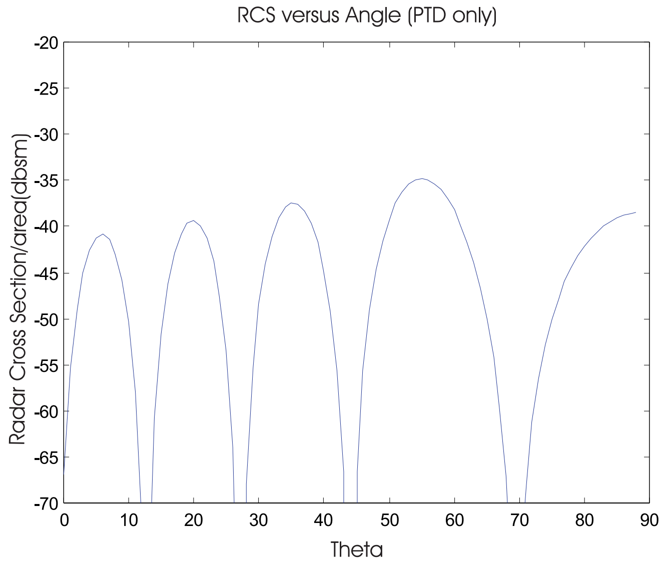

Figure 4.3: Square plate bistatic RCS versus aspect angle(vertical polarization) PTDEEC.

occurs mainly because of the wings on the rear of the fuel tank. Although PO is polarization independent, PTDEEC is not, therefore, results for the fuel tank for horizontal and vertical polarizations differ.

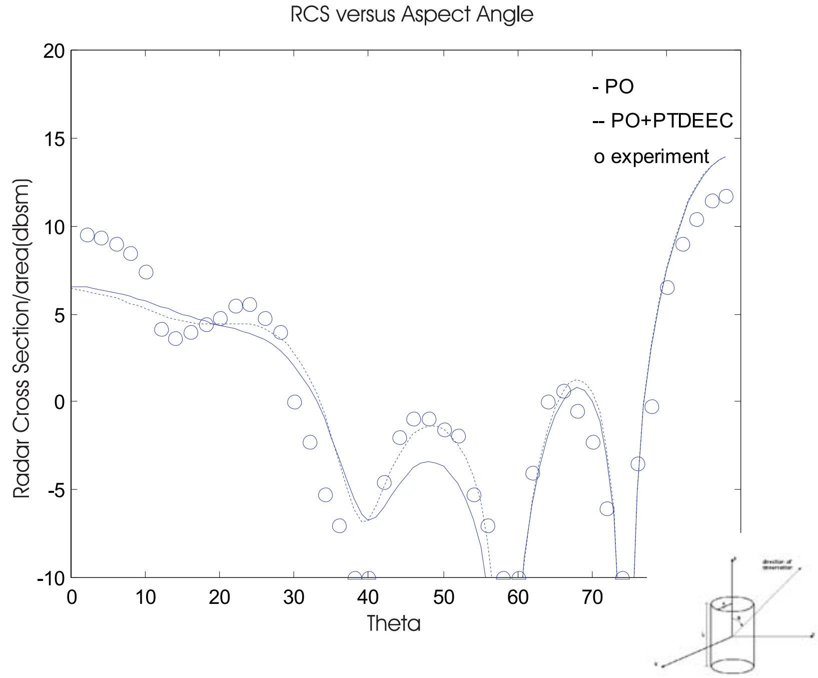

Figure 4.4: Bistatic RCS versus aspect angle(horizontal polarization) for a cylinder. MOM, PO, PO+PTDEEC.

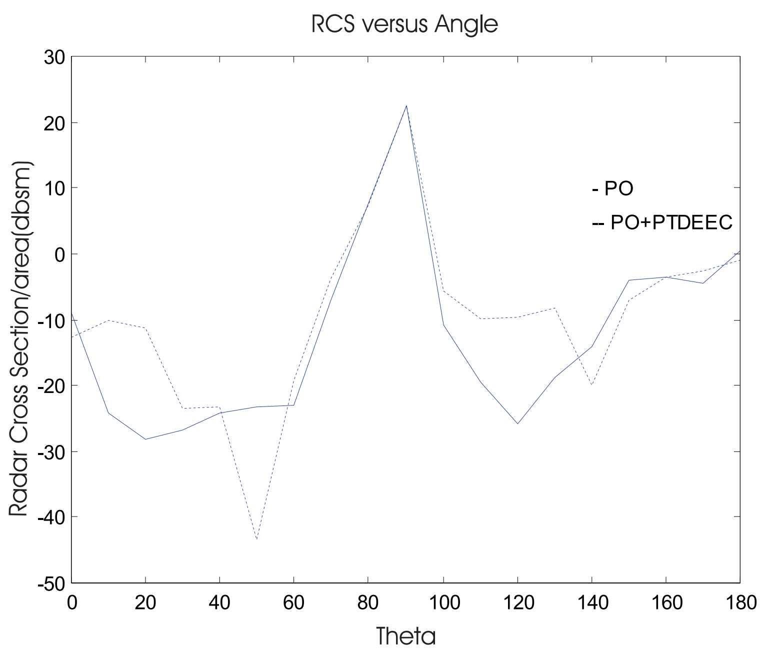

Figure 4.5: Fuel tank RCS versus aspect angle(vertical polarization).

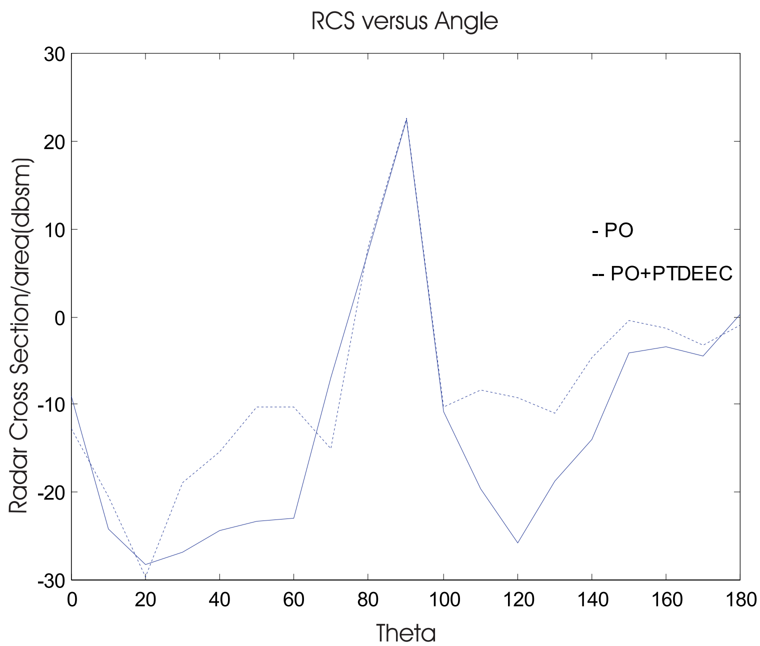

Figure 4.6: Fuel tank RCS versus aspect angle(horizontal polarization).

Chapter 5

PO FOR IMPEDANCE SURFACES

In earlier chapters, scattering from bodies with perfect electric conductor surfaces was considered. Through this chapter, the problem of scattering of a material coated body of arbitrary shape will be discussed. When the coating of the body is thin relative to the radius of curvature of the surface and the free space wavelength, the surface of the target can be approximated to an impedance sheet having an impedance of Z as in equation (5.2). If the thin sheet is primarily conductive, the sheet impedance will be resistive. A thin lossless dielectric sheet will have a purely reactive sheet impedance. The formulation in this section is suitable for lossy or dielectric materials.

When the radius of curvature of the body is electrically large and the coating thickness is much smaller than the radius of curvature, the boundary condition is well defined. The following boundary condition relates the scattered field from a body to the surface impedance Z.

$$-\hat{n} \times \hat{n} \times \bar{E} = \eta_0 Z \hat{n} \times \bar{H} \tag{5.1}$$

Additionally, the magnitude of the refractive index N, and its imaginary part should be large. Under these assumptions the surface impedance can be stated as

$$Z = j\eta tan(Nk_0 d) \tag{5.2}$$

Here η is the intrinsic impedance of the material, k_0 is the free space propagation constant and d is the thickness of the coating layer. Fig. 5.1 illustrates the geometry of the problem for bistatic scattering case.

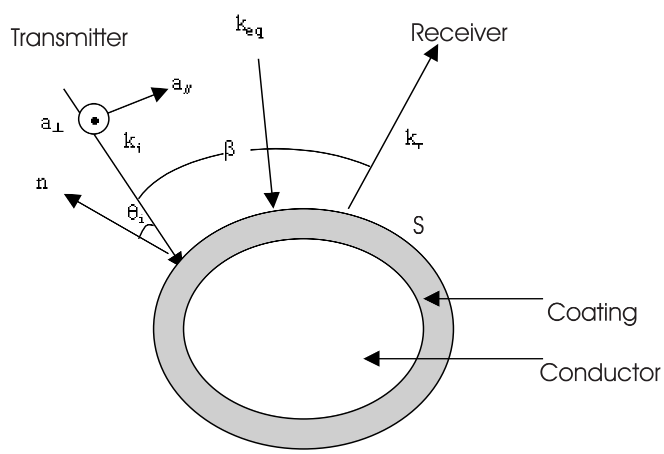

Figure 5.1: Bistatic scattering from a coated object.

Using the surface impedance Z, the parallel and perpendicular reflection coefficients are given as

$$R_{//} = \frac{\frac{Z}{\eta_0} - cos\theta^i}{\frac{Z}{\eta_0} + cos\theta^i} \tag{5.3}$$

$$R_{\perp} = \frac{\frac{Z}{\eta_0} - sec\theta^i}{\frac{Z}{\eta_0} + sec\theta^i} \tag{5.4}$$

5.1 Formulation

Over an illuminated body, it is assumed that both electric and magnetic surface currents are induced. The physical optics approximation for the electric surface current on a body with reflection coefficient matrix R is

$$\bar{J} = \hat{n} \times \bar{H}^t, \tag{5.5}$$

where $\bar{H}_t$ stands for the total magnetic field vector. Using the impedance boundary condition in equation (5.1), the magnetic surface current is found to be

$$\bar{M} = \bar{E} \times \hat{n} = -Z\hat{n} \times \bar{J}. \tag{5.6}$$

The total field can be written in terms of incident field as

$$\bar{H}^t = \hat{n} \times (1 - \bar{\bar{R}})\bar{H}^i. \tag{5.7}$$

The total H-field is given as

$$\bar{H}^t = \left\{ \begin{array}{ll} (1 - R_{//})\bar{H}^i & \text{,parallel polarization} \\ (1 - R_{\perp})\bar{H}^i & \text{,vertical polarization} \end{array} \right\}, \tag{5.8}$$

where the matrix R is

$$\bar{\bar{R}} = \begin{bmatrix} R_{//} & 0 \\ 0 & R_{\perp} \end{bmatrix}. \tag{5.9}$$

$$\bar{H}^t = (1 - R_{//})(\bar{H}^i \cdot \hat{a}_{//})\hat{a}_{//} + (1 - R_{\perp})(\bar{H}^i \cdot \hat{a}_{\perp})\hat{a}_{\perp}, \tag{5.10}$$

where $\hat{a_{//}}$ is the unit vector along the plane of incidence and $\hat{a_{\perp}}$ is the unit vector perpendicular to the plane of incidence.

5.1.1 Solution for a Single Triangle

Scattering from a triangular plate with the surface impedance Z will be considered. The triangular plate lies on the x-y plane. The geometry of problem is illustrated in Fig. 5.2. For a scatterer plate lying on the x-y plane, the plane of incidence is parallel to $\hat{a_\theta}$ and perpendicular to $\hat{a_\phi}$, when the incident wave is a plane wave. Hence, equation (5.10) is simplified to

$$\bar{H}^t = (1 - R_{//})H^i_\theta \hat{a}_\theta + (1 - R_\perp)H^i_\phi \hat{a}_\phi. \tag{5.11}$$

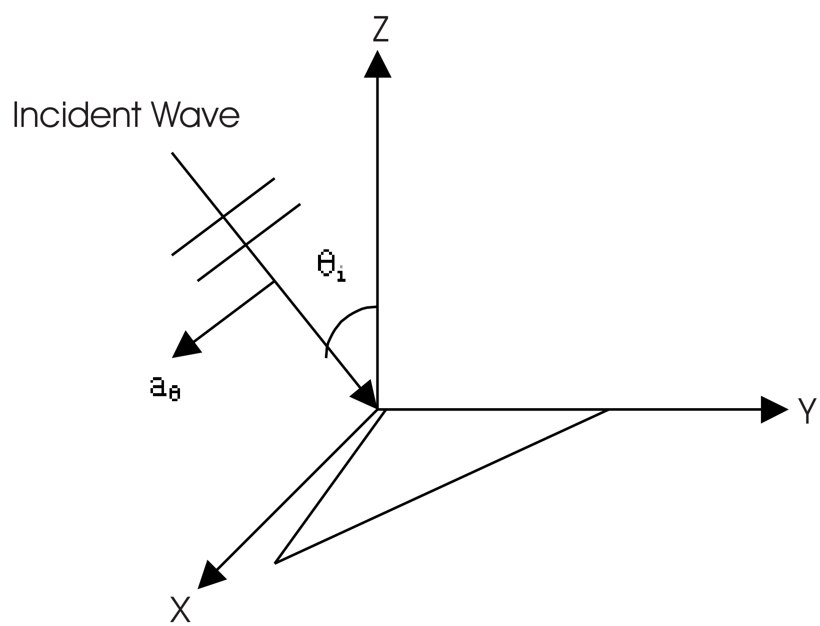

Figure 5.2: Triangular impedance plate orientation.

The scattered E-field can be calculated using the following radiation integral

$$\bar{E}^s = \frac{jw\mu}{4\pi} \int\int \left(\frac{\bar{R} \times \bar{R} \times \bar{J}}{R} e^{-j\bar{k}\bar{R}} + \frac{\hat{k}_r \times \bar{M}}{R} e^{-j\bar{k}\bar{R}}\right) da. \tag{5.12}$$

The following vector algebra will be used:

$$\bar{R} \times \bar{R} \times \bar{J} = \bar{R}(\bar{R} \cdot \bar{J}) - \bar{J}(\bar{R} \cdot \bar{R}). \tag{5.13}$$

Since the surface current is perpendicular to $\bar{R}$, then $\bar{R} \cdot \bar{J} = 0$ and $\bar{R} \cdot \bar{R} = 1$. Hence, the equation (5.13) reduces to $-\bar{J}$. Therefore, equation (5.12) can be written as,

$$\begin{aligned} \bar{E}^s &= -\frac{jw\mu}{4\pi r} e^{-jkr} \int\int (\bar{J} - \hat{k}_r \times \bar{M}) e^{-jk_r r'} da \\ &= -\frac{jw\mu}{4\pi r} e^{-jkr} \int\int ((\hat{n} \times \bar{H}^t) - \hat{k}_r \times (-Z\hat{n} \times \bar{J})) e^{-jk_r r'} da \\ &= -\frac{jw\mu}{4\pi r} e^{-jkr} \int\int ((\hat{n} \times \bar{H}^t) - \hat{k}_r \times (-Z\hat{n} \times \hat{n} \times \bar{H}^t)) e^{-jk_r r'} da \end{aligned} \tag{5.14}$$

Using $\bar{H}^i = \frac{\hat{k}^i \times \bar{E}^i}{\eta_0}$ we get,

$$H^i_\phi = -\frac{E^i_\theta}{\eta_0}, \tag{5.15}$$

$$H^i_\theta = -\frac{E^i_\phi}{\eta_0}. \tag{5.16}$$

Using equation (5.11) and the relationships (5.15), (5.16) in equation (5.14), the two components for the scattered field of a particular triangular mesh in our model are found to be

$$\begin{aligned} E^s_\theta = \frac{-jke^{-jkr}}{4\pi r} \int\int & (E^i_\theta (1 - R_{//})(cos\theta cos(\phi - \phi^i) - Z) \\ & + E^i_\phi (1 - R_\perp) cos\theta cos\theta^i sin(\phi - \phi^i)) e^{-k_{eq} r} da, \end{aligned} \tag{5.17}$$

$$\begin{aligned} E^s_\phi = \frac{-jke^{-jkr}}{4\pi r} \int\int & (-E^i_\theta (1 - R_{//}) sin(\phi - \phi^i) \\ & + E^i_\phi (1 - R_\perp)(cos\theta^i cos(\phi - \phi^i) + Z(sin\theta sin\theta^i - 1))) e^{-k_{eq} r} da. \end{aligned} \tag{5.18}$$

Unit normal is taken as, $\hat{n} = \hat{z}$. The equations (5.17) and (5.18) can be written in matrix form as

$$\begin{bmatrix} E^s_\theta(r,\theta,\phi) \\ E^s_\phi(r,\theta,\phi) \end{bmatrix} = \begin{bmatrix} F_{11}+Z & F_{12} \\ F_{21} & F_{22}+Z(sin\theta sin\theta^i - 1) \end{bmatrix} \begin{bmatrix} (1-R_{//}) & 0 \\ 0 & (1-R_{\perp}) \end{bmatrix} \begin{bmatrix} E^s_\theta \\ E^s_\phi \end{bmatrix} \frac{2I_0}{\eta}\frac{jw\mu}{4\pi r}e^{-jkr}, \quad (5.19)$$

where the F_{11}, F_{12}, F_{21} and F_{22} are as given in equations (2.32), (2.33), (2.34) and (2.35) respectively. Notice that the PO scattering matrix, F, in PEC case is modified for dielectric case. These new components in PO scattering matrix are due to the extra induced magnetic current.

5.2 Applications and Comparisons

The monostatic RCS for a 1m square plate, which lies on the x-y plane, is calculated. The PEC and the dielectric cases are compared. Figures 5.3 and 5.4 show the monostatic RCS versus aspect angle results at 700MHz for the square plate for horizontal and vertical polarizations, respectively. The red plots show the PEC sheet case. For a PEC surface, the result is the same for both polarizations. The blue plots depict the impedance plate case, where the normalized impedance of the coating material is 0.6. It is observed that the RCS decreases with respect to the PEC case and the results are different for different polarizations. The results for the square plate are compared with the results in [17].

As an other example, fuel tank is studied. Fuel tank is assumed to have material coating over its surface. The surface of the fuel tank is approximated as an impedance surface with impedance Z under the assumptions of thin material coating and large radius of curvature with respect to the coating thickness. Fig.

RCS versus Aspect Angle

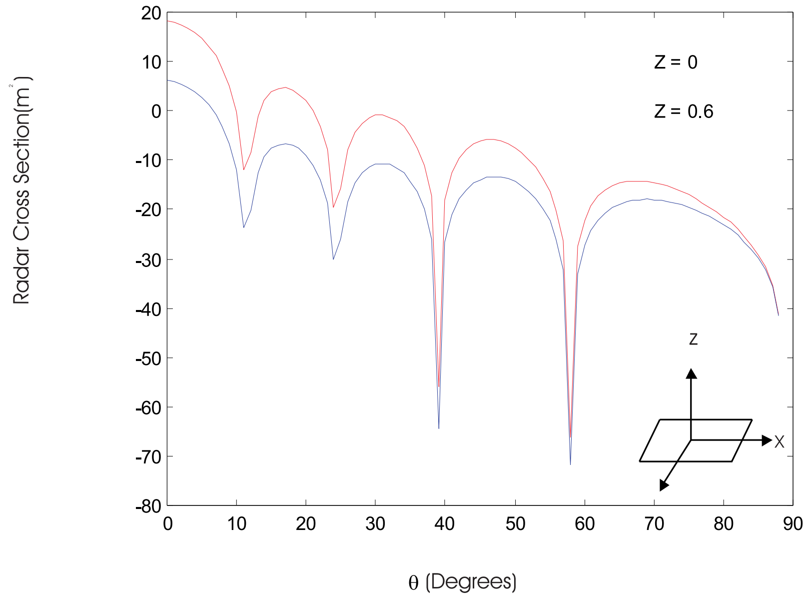

Figure 5.3: RCS of a square sheet of 1m at 700MHz(Horizontal polarization).

5.5 and 5.6 present the monostatic RCS versus aspect angle results of the fuel tank for the horizontal and vertical polarizations, respectively. The operating frequency is 13GHz. The normalized impedance is taken as 0.6 and the RCS results are compared with the RCS results of PEC case, where surface impedance is 0. Fig. 5.7 and 5.8 present the monostatic RCS versus frequency results of the fuel tank for the horizontal and vertical polarizations respectively. The aspect angles are; $\theta = 45°$ and $\phi = 160°$. The red plots again depict the PEC sheet case. The blue plots show the impedance sheet case, where the normalized impedance of the coating material is 0.6. In Figures 5.7 and 5.8, the green plots present the RCS result for the dielectric case with the normalized impedance equal to 1.5. It is observed that the RCS decreases as the impedance increases and the RCS data is different for different polarizations in case of non-zero surface impedance.

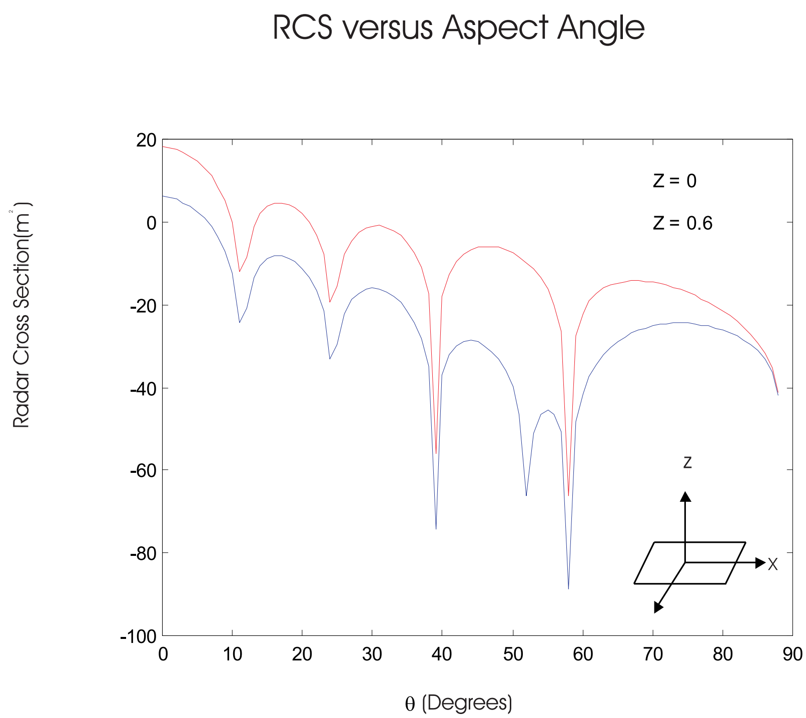

Figure 5.4: RCS of a square sheet of 1m at 700MHz(Vertical polarization).

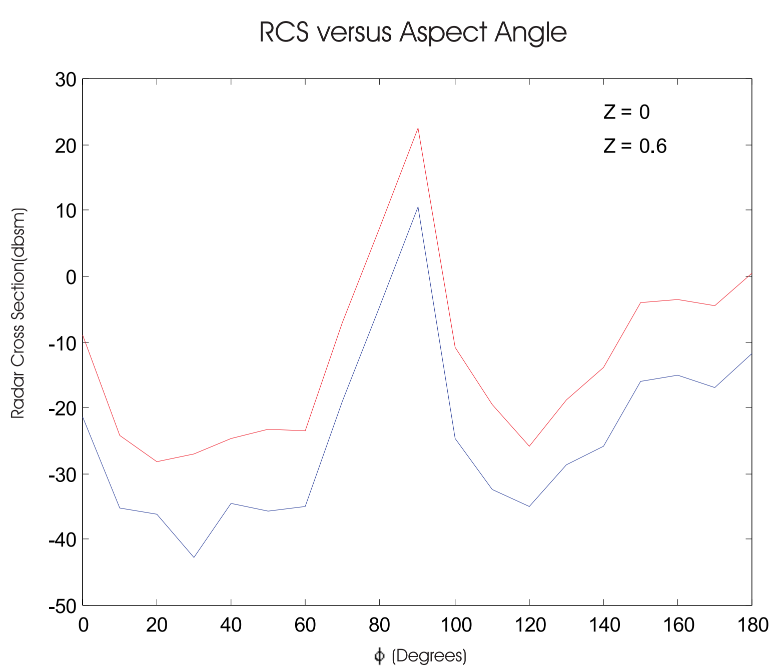

Figure 5.5: RCS of fuel tank at 13GHz($\theta = 45°$, Horizontal polarization).

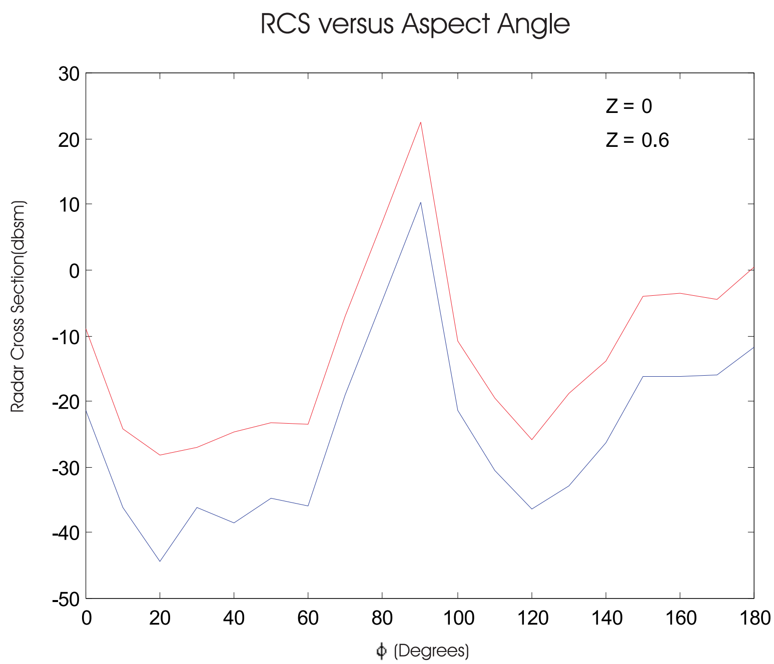

Figure 5.6: RCS of fuel tank at 13GHz($\theta = 45°$, Vertical polarization).

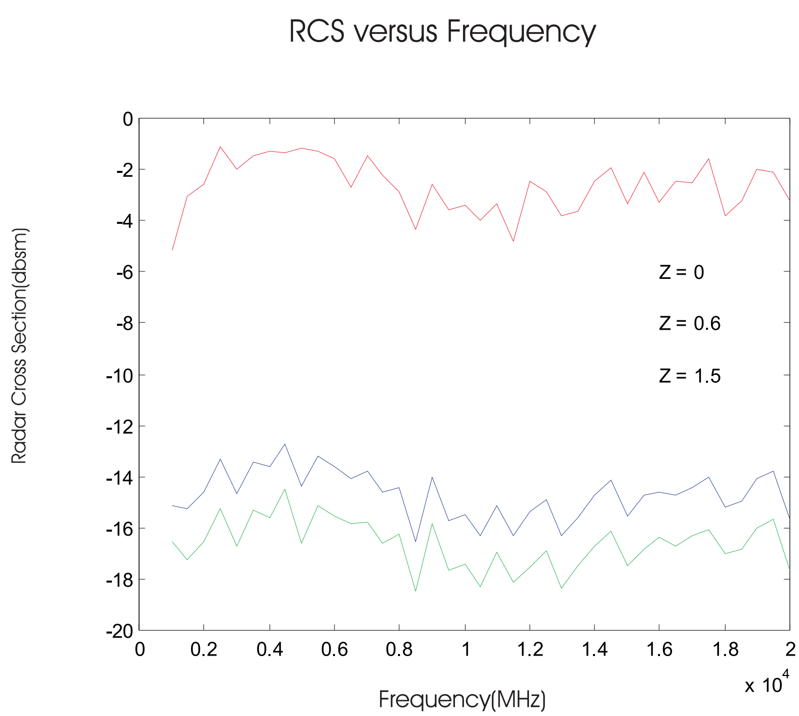

Figure 5.7: RCS of fuel tank at $\theta = 45°$, $\phi = 160°$ (Horizontal polarization).

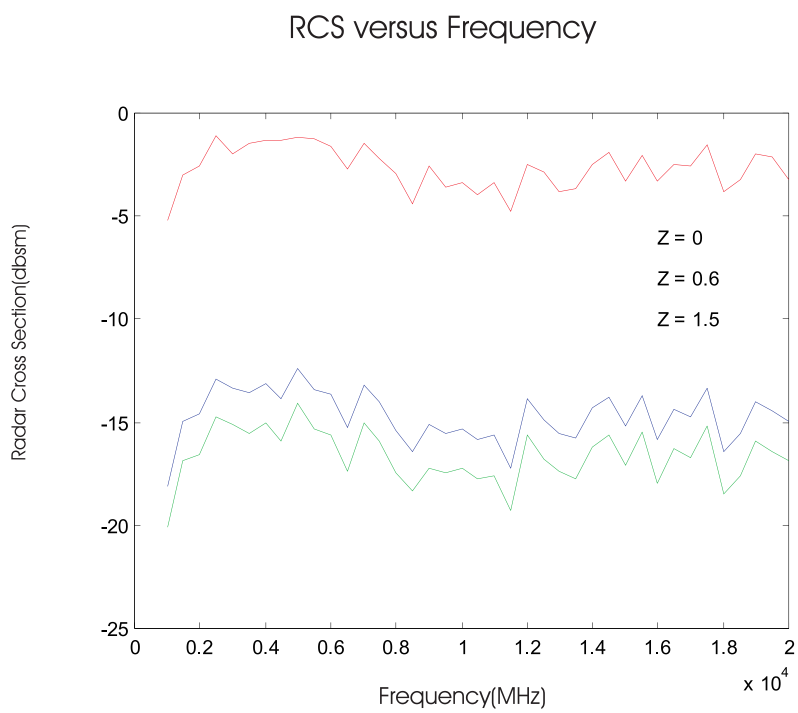

Figure 5.8: RCS of fuel tank at $\theta = 45°$, $\phi = 160°$ (Vertical polarization).

Chapter 6

SHADOWING

When an electromagnetic wave is incident on a body, part of its surface is illuminated and the rest is dark, depending on the direction of propagation with respect to the body. Additionally, some parts of the body may be shadowed by other parts. For example, the wings of a plane may shadow part of the body for some illumination angles. In the PO solution, the contributions from these shadowed regions should be discarded from the RCS calculations, so that the scattered field due only to the illuminated regions should contribute to the RCS.

In the results of previous chapters, shadowing was not included. A simple illumination test applied to each triangular mesh, to explore if this plate is in illuminated region or not. The test calculates the dot product of surface unit normal and the propagation vector. If the dot product is smaller than 0, then this triangular plate is said to be illuminated and the PO contribution is added to the total scattered field. Otherwise the contribution from this particular triangle is discarded.

There are many algorithms used in order to find the shadowed regions. In this thesis, an algorithm similar to Möller-Trumbore [19] is used. All of the triangles in the plate model of the scatterer body are checked if they shadow any other triangles [20]. The shadowing test methodology is described in the following section.

6.1 Methodology

At the beginning, the first triangle is taken and all the other triangles are tested if this triangle is shadowed by the others or not. A ray, passing through a predefined point of the first triangle and in the direction of propagation, is defined. The main idea is to check whether the ray passing through a pre-defined point on the shadowing triangle crosses the second triangle. The intersection test is applied four times for the rays passing through three corners and the mid-point of the shadowing triangle each. If at least one of the rays intersect the second triangle, one of the triangle is in shadow of the other. A group of triangles may be shadowed by a single triangle. The situation is illustrated in Fig. 6.1.

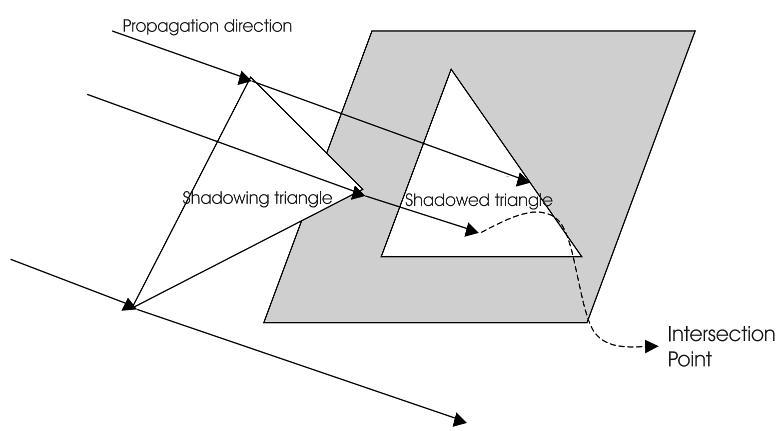

Figure 6.1: Illustration of shadowing and shadowed triangles.

One by one each triangle is tested, using the same triangle taken initially. The shadowing and shadowed triangles are saved in a shadow array. More than one triangle may be in shadow because of a single triangle, depending on the shape of the scatterer. Calculating the distance from each triangle of the shadow array to a distant point in the propagation direction, the nearest one is found to be the shadowing triangle and all the others are shadowed triangles. Induced currents, hence the scattered field from shadowed triangles are not considered. This way, the inaccuracy in the RCS calculation due to the effect of shadowing is minimized.

6.2 Ray Intersection Algorithm

The ray that passes through the triangle is in the same direction as the propagation direction and a particular point on the shadowing triangle resides on this ray. The ray R(t) with origin O and normalized direction P, which is the propagation vector in our case is given by the following formula:

$$\bar{R}(d) = \bar{O} + d\bar{P}, \tag{6.1}$$

where d is the distance to the plane in which the triangle lies.

Any point on the plane on which the second triangle resides can be expressed by the following formula:

$$\bar{P}(s,t) = \bar{P}_1 + s(\bar{P}_2 - \bar{P}_1) + t(\bar{P}_3 - \bar{P}_1), \tag{6.2}$$

where $\bar{P}_1$, $\bar{P}_2$ and $\bar{P}_3$ are corner vectors of the second triangle and s and t represent the coordinates inside the triangle. s and t are the barycentric formulas and must fulfill conditions in (6.7).

The intersection point of the propagating ray on the plane of second triangle is found by equating the ray and the plane formula as

$$\bar{P}_i = \bar{P}_1 + s_i(\bar{P}_2 - \bar{P}_1) + t_i(\bar{P}_3 - \bar{P}_1) = \bar{O} + d\bar{P}, \tag{6.3}$$

where s_i and t_i are the particular barycentric coordinates of the intersection point on the plane where the second triangle lies.

Then,

$$\bar{P}_i - \bar{P}_1 = \bar{O} + d\bar{P} - \bar{P}_1 = s_i\bar{U} + t_i\bar{V} = \bar{W}. \tag{6.4}$$

The above equation can be rewritten in matrix form as

$$[-\bar{P}, \bar{U}, \bar{V}] \begin{bmatrix} d \\ s \\ t \end{bmatrix} = \bar{O} - \bar{P}_1. \tag{6.5}$$

The equation in (6.5) can be thought of geometrically as translating the triangle to the origin and transforming it to a unit triangle in y and z with the ray direction aligned with x, as illustrated in Fig. 6.2, where $M = [-\bar{P}, \bar{U}, \bar{V}]$.

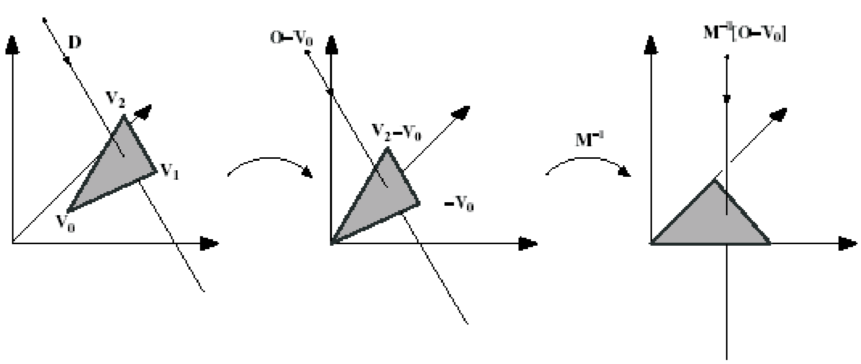

Figure 6.2: Triangle translation and change of the case of the ray origin.

From (6.4) the barycentric coordinates of the intersection point s_i and t_i are solved to be

$$
\begin{aligned}
s_i &= ((\bar{U}.\bar{V})(\bar{W}.\bar{V}) - (\bar{V}.\bar{V})(\bar{W}.\bar{U}))/((\bar{U}.\bar{V})(\bar{U}.\bar{V}) - (\bar{V}.\bar{V})(\bar{U}.\bar{U})), \\
t_i &= ((\bar{U}.\bar{V})(\bar{W}.\bar{U}) - (\bar{U}.\bar{U})(\bar{W}.\bar{V}))/((\bar{U}.\bar{V})(\bar{U}.\bar{V}) - (\bar{V}.\bar{V})(\bar{U}.\bar{U})). \quad (6.6)
\end{aligned}
$$

The intersection point is decided to be inside the triangle, if the following conditions hold:

$$
\begin{aligned}
s_i &\geq 0, \\
t_i &\geq 0, \\
s_i + t_i &\leq 1. \quad (6.7)
\end{aligned}
$$

Taking one of the triangles, each triangle is tested to determine whether the triangles reside on the same plane, that is, whether they are parallel. To accomplish this test, the propagation vector $\bar{P}$ cross producted with the normal vector of the second triangle. If the result is sufficiently close to 0, then the two triangles are assumed to lie on the same plane and they do not shadow each other.

Afterwards the conditions in equation (6.7) are checked. If the conditions in equation (6.7) hold, then it is concluded that one of the triangles shadow the other.

6.3 Results

In order to check for the correctness of the shadowing algorithm, A geometry of two 1m square sheets on top of each other as in Fig. 6.3 is considered. The distance between the square sheets is 0.001m, even though they appear to be further apart in Fig. 6.3 for illustrative purposes.

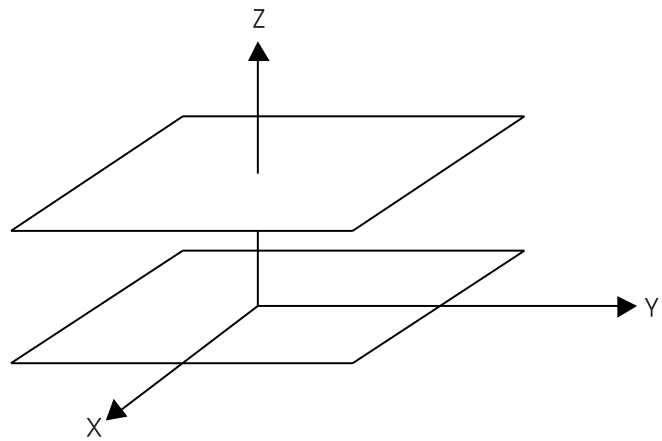

Figure 6.3: Two 1m square sheets on top of each other.

Fig. 6.4 shows the RCS data for square plate of 1 m at 1GHz. The straight line represents only the one square data and the dashed line represents the data for two square sheets on top of each other, where the lower one is shadowed by the upper one. The small error around 90° is due to the small distinction between the squares. Some errors may also occur due to the decision on shadowing by only one of the four points on the triangle.

Fig. 6.5 represents the RCS versus aspect angle for the fuel tank at 13GHz. The dashed line plot represents the RCS data, where the shadowing algorithm is applied and the straight line plot represent the RCS data, where shadowing is not used. It is observed that shadowing is effective around 180°, due to shadowing of the wings of the fuel tank. Shadowing is not as effective for the fuel tank as expected.

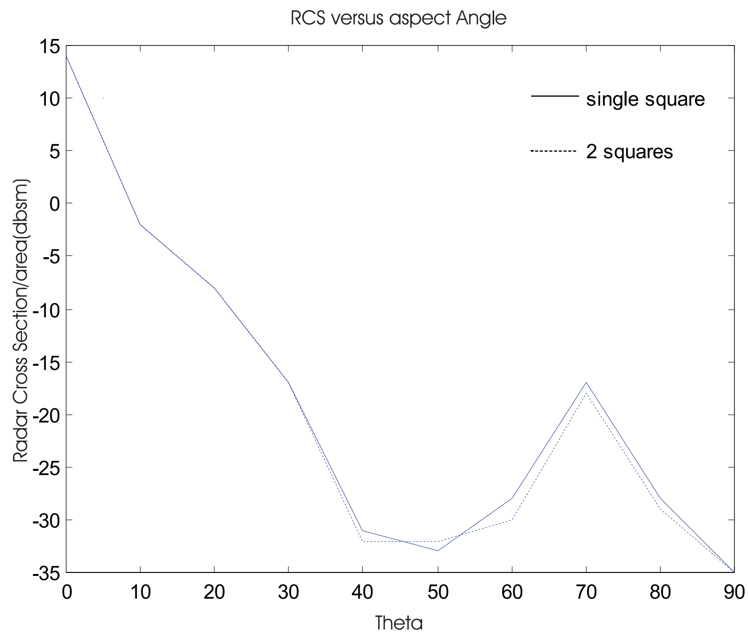

Figure 6.4: Two 1m square sheets on top of each other.

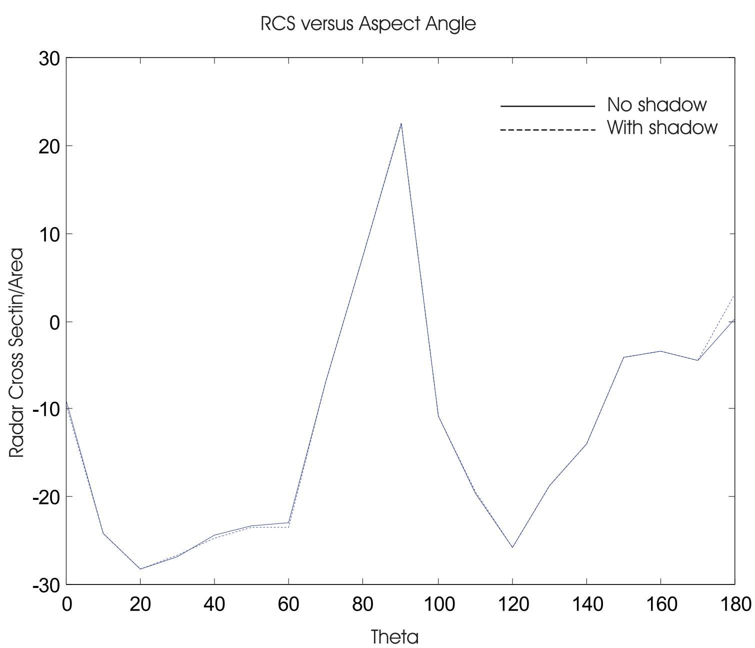

Figure 6.5: RCS of the fuel tank at 13GHz.

Chapter 7

FLASH POINT ANALYSIS

According to the high frequency phenomena, only some parts of the scatterer contribute to the scattered field. These parts may be edge, corner or specular reflection point. When a wave is incident on an object, currents are induced over the entire scattering surface S, but those in the vicinity of the specular points(the Fresnel zones) are the dominant contributors to the scattered field. Many high frequency diffraction techniques such as GTD, UTD and PTD utilize this local phenomena. Although the Physical optics currents are also locally defined, Physical Optics express the total field as the integration of all the contributions. These localized PO surface currents can be visualized.

7.1 Visualization of Surface Currents Due to Scattering and Diffraction

PO approximates the induced surface current as

$$\bar{I}^{PO} = \hat{n} \times \bar{H}^i, \tag{7.1}$$

where $\hat{n}$ is the outer unit normal vector and H^i is the incident field vector.

The far scattered field is calculated by the surface integration of PO current in equation (7.1) over the lit region. According to the high frequency phenomena, electromagnetic waves due to current distributions from every part of the surface, do not contribute to the total scattered field for a particular observation point, since the adjacent currents cancel each other. With the aid of the visualization, only the dominant part of the surface current is extracted.

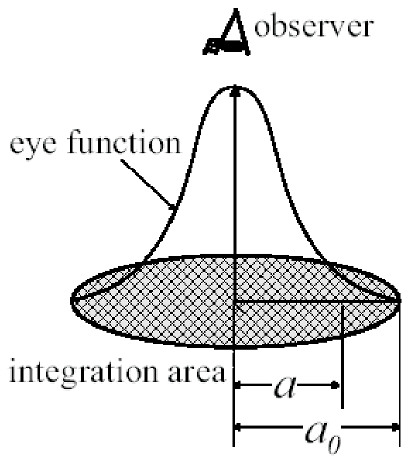

Figure 7.1: Eye function.

The eye function in equation (7.2) and Fig. 7.1 is used for visualization. The PO currents weighted by the eye function is integrated over the surface of the scatterer. This way, adjacent currents due to rapid change in high frequency cancel each other and only the dominant currents survive. Brightness at a particular point is given by the surface radiation integral of the PO currents weighted with the eye function with the center of the eye function residing at that point.

$$eye(a) = \begin{cases} cos\left(\frac{a}{a_0}\pi\right) + 1 & (a \leq a_0), \\ 0 & (a > a_0) \end{cases} \tag{7.2}$$

Selection of the radius of the eye function a_0 is important. If the radius of the eye function exceeds the second fresnel zone, then the brightness at that particular point converges. Hence the radius of the eye function should be selected larger than the radius of second fresnel zone. The eye function radius and fresnel zone relation can be observed in Fig. 7.2.

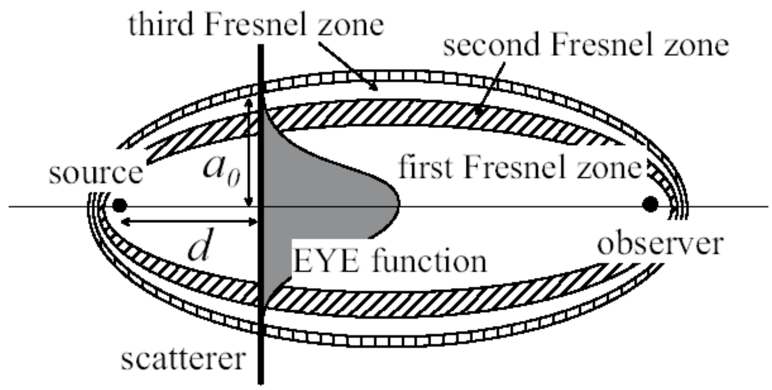

Figure 7.2: Fresnel zone and eye function illustration.

The second Fresnel zone radius is found by equation (7.3).

$$r_2 = \sqrt{\frac{2\lambda d1 d2}{d1 + d2}}, \tag{7.3}$$

where d1 and d2 are the distances to the source and the observation points.

Since in our case, the incident wave is a plane wave, a large value should be selected for the radius of the eye function. Approximating the source and observation distances as 1000λ each the radius of the second fresnel zone is calculated to be 44λ. Therefore the radius of the eye function is selected as 50λ.

7.2 Square Plate

The first example of visualization is a conductive square plate. The situation is illustrated in Fig. 7.3. The dimension of the square plate is 1m and the operating frequency is 90Ghz. Flash points are analyzed for backscattering case.

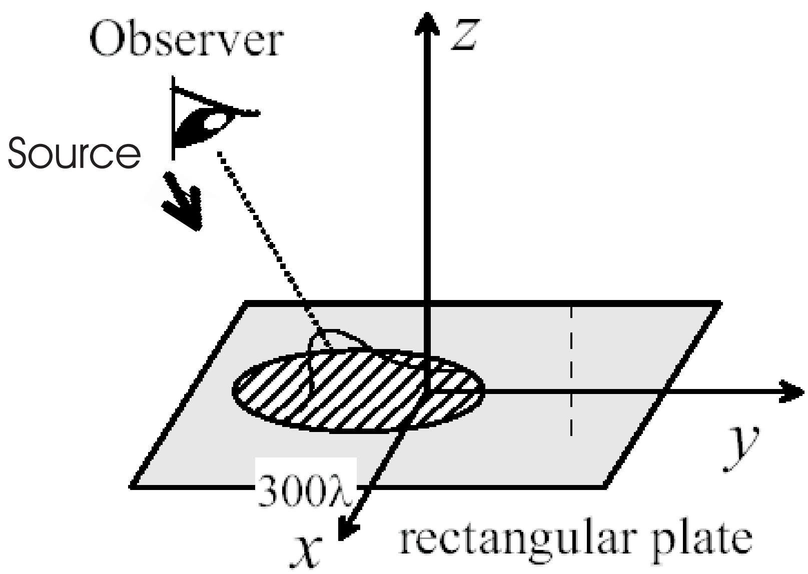

Figure 7.3: Model of visualization.

Figure 7.4 depicts the integration result over the square. The colorbar on the right hand side of the square represent the brightness increasing from dark blue towards red. The source and the observation angles are 0°.

The inner bright region represents the reflection point. The less bright regions around the edges of the square represent the diffraction currents. Since the incident wave is a plane wave, nearly all of the surface of the square plate is seen to be bright, which indicates that the wave is reflected by all of the surface. Additionally, there is some brightness around the edges due to diffraction. Since the incidence angle is 0° for Fig. 7.4, the reflection points are brighter than the diffraction points.

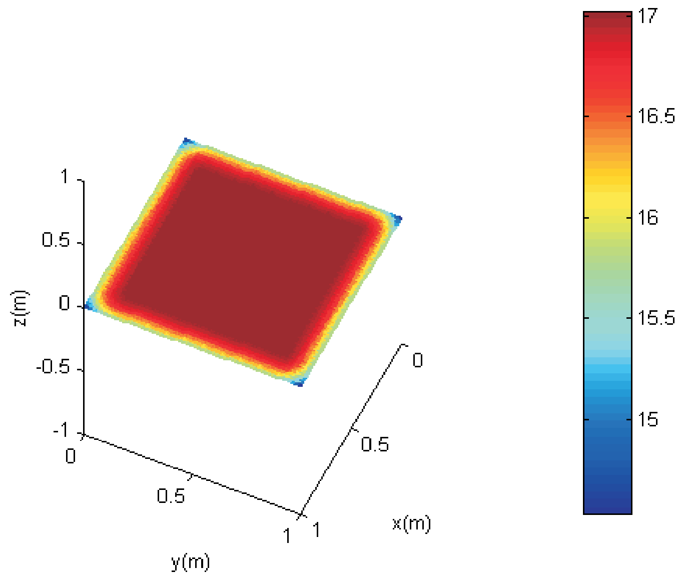

Figure 7.4: Flash point visualization of 300λ square plate for $\phi = 45°, \theta = 0°$.

Figure 7.5 represents the flash points for the incidence angle of 45°. The effect of corner diffraction is observed around the corners, where there were no currents for the 0° case. In addition it is observed that reflection currents for 45° case are less effective than the 0° case.

Figure 7.6 represents the flash points for the incidence angle of 70°. This time the diffraction currents are more effective than the reflected currents, which was expected. The diffraction is more effective as the propagation vector is more parallel to the plane of the square plate.

The second example for flash point visualization is a conducting sphere with radius 1m. Figure 7.7 represents the brightness over the sphere, where both the incidence and observation angles are $\theta = 90°$, $\phi = 45°$ and the frequency is 1GHz. The brightest region around the incidence angles represents the GO reflection. Figure 7.8 represents the brightness over the same sphere, this time for bistatic case. The incidence angles are $\theta_i = 90°$, $\phi_i = 45°$ and the observation angles are $\theta_s = 45°$, $\phi_s = 45°$ and frequency is the same. The sphere is less bright with

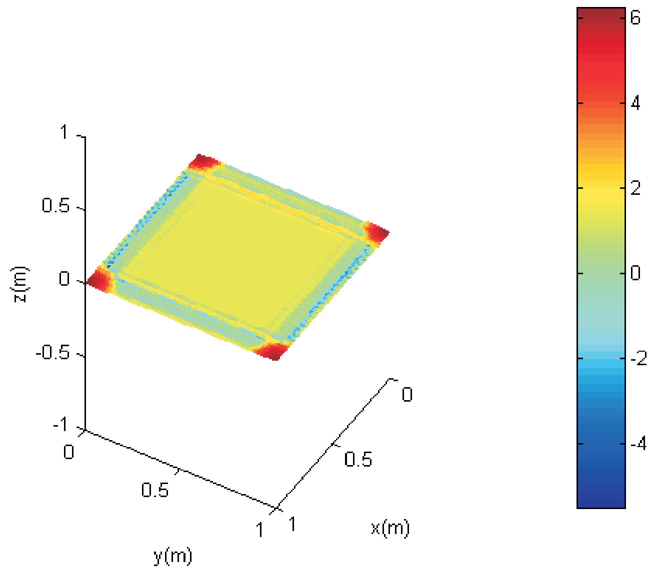

Figure 7.5: Flash point visualization of 300λ square plate for $\phi = 45°, \theta = 45°$.

respect to the monostatic case. It is concluded that reflection is less effective at an observation angle different than the incidence angle.

The flash point analysis for horizontal and vertical polarizations both gave the same result, which is known for physical optics integration.

Using the flash point visualization, localized reflected and diffracted currents are extracted. For our case of plane wave incidence, the reflected and diffracted currents are observed all over the surface. For cases where the source is not a plane wave, more localized currents are expected. Although PO technique is fast compared to MOM, RCS calculations for very large objects such as ships, may take long period of time. Localizing the important contributions of the surface current, and calculating the PO integral around these regions may shorten the calculation period.

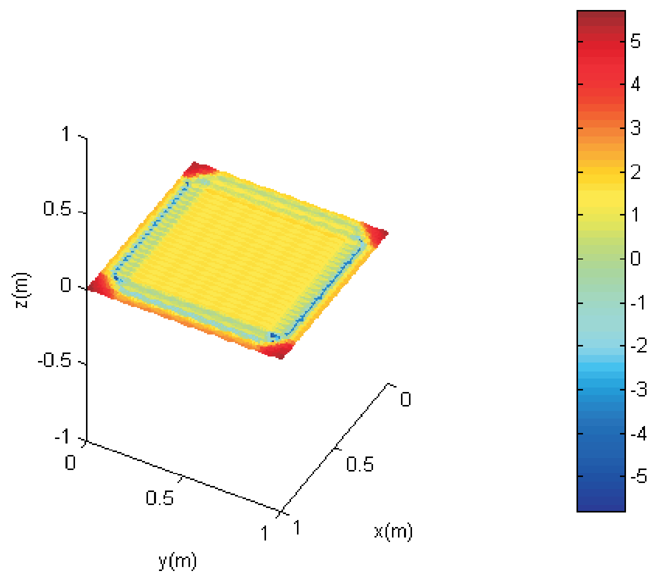

Figure 7.6: Flash point visualization of 300λ square plate for $\phi = 45°, \theta = 70°$.

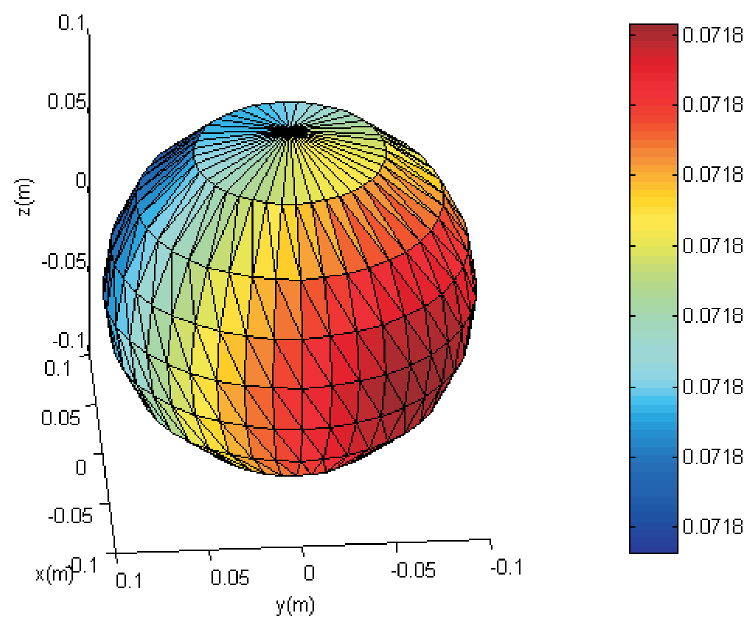

Figure 7.7: Flash point visualization of sphere with radius of 1m for $\phi = 45°, \theta = 90°$.

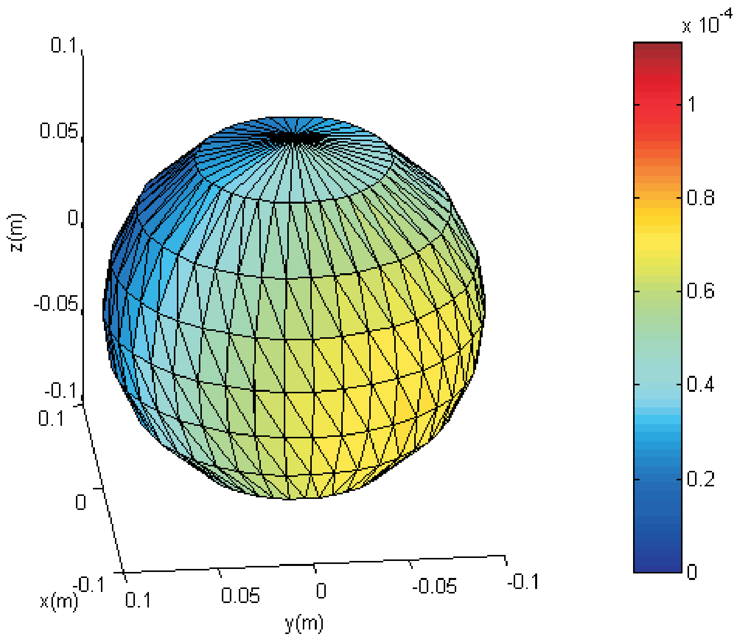

Figure 7.8: Flash point visualization of sphere with radius of 1m for $\phi_i = \phi_s = 45°, \theta_i = 90°, \theta_s = 45°$.

Chapter 8

CONCLUSIONS

Physical Optics (PO) and Physical Theory of Diffraction (PTD) are used to calculate RCS of targets with arbitrary shapes, with perfectly conducting or impedance surfaces. A computer program has been written in Fortran for the computations.

The targets are modeled in triangular meshes for easier computations. The program includes a mesh generator algorithm for basic shapes. Additionally triangular mesh models generated by graphical tools can be exported, and RCS of any target with these models can be calculated.

PO is one of the high frequency techniques, and PTD is correction to PO. For high frequency Radar Cross Section(RCS) computations, PO gives faster results for large targets. PO approximates the induced surface currents, the Geometric Optics(GO) currents, and integrates them over the surface of the scatterer to obtain the scattered field. Hence, PO eliminates the infinities of GO due to flat and simply curved surfaces.

In our case, the PO integral is calculated analytically. This gives the freedom of choosing the sizes of the triangular meshes, so that the Radar Cross Section

(RCS) of targets that have any shape, modeled as triangular plates with any size, can be calculated. This method is applicable for targets having flat surfaces, such as ships, buildings, etc. For curved surfaces, selection of large meshes may change the shape of the surface, therefore calculated RCS data may become inaccurate. Additionally, by using analytical approach to the surface integral, faster computation time is achieved.

In earlier calculations, not to have phase change over a particular plate, the meshes were generated small enough with respect to λ. By this selection, the phase was taken to be constant over the surface and faster computing time was achieved. But, when exporting triangular model of a target, the mesh size may not be selectable and the assumption of constant phase may not work for large meshes; whereas analytic approach is even more efficient for large meshes, independent of the operating frequency. A performance table of the program is given in Figure 8.3 in Appendix A.

PO approximation can be rendered more accurate by adding the effect of diffraction. PTD is used to account for diffraction. First order diffraction is considered only, since higher order ones are not effective for targets that have large surfaces. The fringe wave (FW) currents, caused by diffraction around the edges, are added to GO current approximation. PTD is the superposition of the PO field and the field caused by the equivalent edge currents, the edge diffracted fields. The method of Equivalent Edge Currents (EEC) depends on finding the currents that would, when integrated along the edge, give a known value of radiated field.

The computer program is used to calculate the RCS of some basic shapes, such as a sphere, a cylinder, a square plate. The results are compared with the ones available in literature. The computations are also applied to the fuel tank of F-16 airplanes. The results are compared with the ones, where GO method is used. It is seen that PO and GO give similar results for RCS calculations of the fuel tank model. As mentioned above, GO traces all of the incident and reflected rays, whereas PO only calculates the simple surface integral. Hence PO technique is easier to apply when compared to GO, especially in the case of objects modeled as flat plates.

PO is also applied to the impedance surfaces. A conducting body with material coating can be approximated as impedance sheet under the assumption of thin coating with respect to the radius of curvature and impenetrable surface. Applying the PO for targets that have impedance surfaces yields RCS results that are lower than the results of perfectly conducting surfaces. Therefore, RCS of conducting targets can be decreased by material coating. Although the scattered field is polarization independent for perfect conductors, the results for horizontal and vertical polarizations are different for impedance surfaces.

The scattered field and the diffraction phenomena by PO are visualized using flash points. Dominant currents due to reflection and diffraction are visualized over a square plate for plane wave incidence. Hence, the local property of high frequency scattering is demonstrated.

In order to obtain more accurate results for targets that have more complicated surfaces; such as ships, buildings etc, shadowing algorithm has been implemented and tested. The effect of shadowing has been calculated for fuel tank of a F-16 plane.

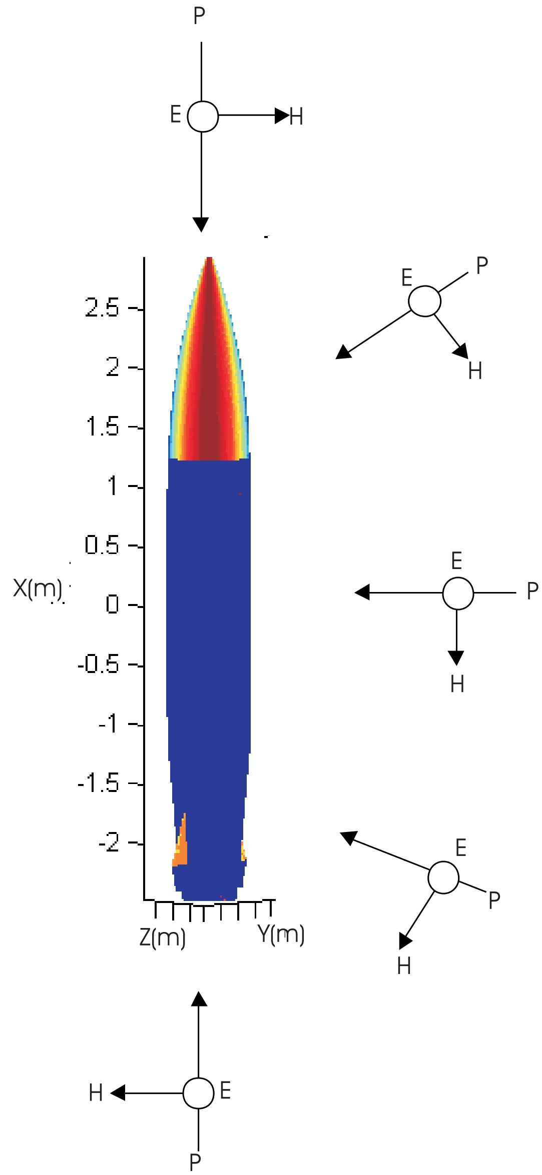

Figure 8.1: Vertical polarization

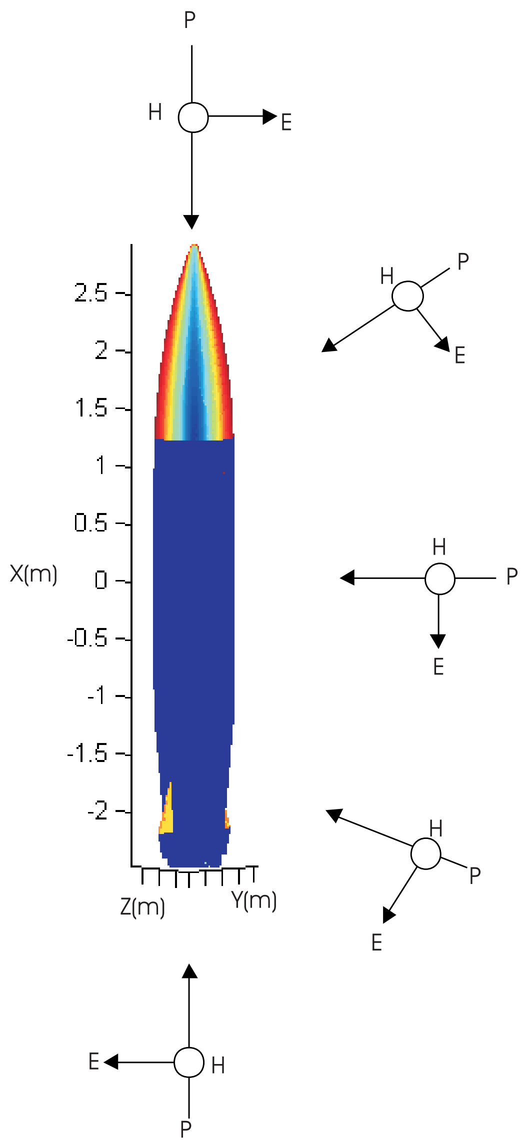

Figure 8.2: Horizontal polarization

	Cylinder	Square	Fuel Tank
# meshes	**95904**	**200**	**136619**
Mesh size	**0.0005m^2**	**0.005m^2**	**<0. 0005m^2**
Calculation Time	**2seconds**	**1second**	**5 seconds**

Figure 8.3: Mesh count versus performance of the program

Bibliography

[1] R. F. Harrington, *Time Harmonic Electromagnetic Fields*, McGraw-Hill, New York, 1961.

[2] P. Ya Ufimtsev, "Method of Edge Waves in the Physical Theory of Diffraction", (from the Russion "Method Krayevykh Voin V Fizichenskoy Theorii Diffraktsii", *Izd-Vo Sov. Radio,pp.1-243, 1962.)*, Translation prepared by the U.S. Air Force Foreign Technology Division, Wright-patterson AFB, OH, Sept. 1971.

[3] D. I. Butorin, P. Ya Ufimtsev, *Sov. Phys. Acoust.*, Vol.32, No.4, July-Aug. 1986.

[4] D. A. McNamara, C. W. I. Pistorius, J. A. G. Malherbe, *Introduction to the Uniform Theory of Diffraction*, Artech House, Boston, 1990.

[5] P. H. Pathak, *Techniques for High Frequency Problems*, Antenna Handbook Volume I, Chapter 4, Van Nostrand Reinhold, New York, 1993.

[6] T. B. Hansen, "Corner Diffraction Coefficients for the Quarter Plate", *IEEE Transactions on Antennas and Propagation*, Vol.39, No.7, pp.976-984, July 1991.

[7] J.H. Richmond, "The Basic Theory of Harmonic Fields, Antennas and Scattering", *Ch. 4The Radiation Integrals. Ohio State University Electro Science Laboratory*, unpublished notes, 1985.

[8] R. Paknys, C. W. Trueman, "High Frequency RCS Prediction for Vehicles Treated with RAM", *Concordia University*, September 2002.

[9] Eugene F. Knott, John F. Shaeffer, Michael T. Tuley, *Radar Cross Section*, Chapter 6, Artech House, Mass., 1985.

[10] R. F. Millar, "An Approximate Theory of the Diffraction of an Electromagnetic Wave by an Aperture in a Plane Screen", *Proc. Inst. Elect. Eng.*, Vol.103C, p.177-185, 1956.

[11] K. M. Mitzner, *Incremental Length Diffraction Coefficints*,Aircraft Div., Northrop Corp., Tech. Rep. AFAL-TR-73-296, Apr. 1974.

[12] A. Michaeli, "Equivalent Edge Currents for Arbitrary Aspects of Observation", *IEEE Transactions on Antennas and Propagation*, Vol.32, No3, p.252-258, March 1984.

[13] A. Michaeli, "Elimiation of Infinities in Equivalent Edge Currents, Part I:Fringe Current Components", *IEEE Transactions on Antennas and Propagation*, Vol.34, No7,p.912-918, July 1986.

[14] A. Arif Ergin, *Maske Projesi Benzetim Çalışması* 3*. Aşama Raporu* , Rev.00, 2003.

[15] V. Stein, "Application of Equivalent Edge Currents to Correct the Backscattered Physical Optics Field of Flat Plates", *Applied Computational Electromagnetics Society Journal*, Vol.7, No1, 1992.

[16] J. F. Shaeffer, "EM Scattering from Bodies of Revolution with Attached Wires", *IEEE Transactions on Antennas and Propagation*, Vol.AP-30, no.3, pp.426-431, May 1982.

[17] Debra Wilkis Hill, Chung-Chi Cha, "Physical Optics Approximation of the RCS of an Impedance Surface", , pages 416-419, 1988.

[18] Raymond J. Luebbers, Karl Kunz, "FDTD Modeling of Thin Impedance Sheets", *IEEE Transactions on Antennas and Propagation*, Vol.4, No3, 1992.

[19] T. Möller, B. Trumbore, "Fast, Minimum Storage Ray-triangle intersection", *Journal of Graphics Tools*, 2(1):21-28, 1997.

[20] T. Möller, "A Fast Triangle-Triangle Intersection Test", *Journal of Graphics Tools*, 2(2), 1997.

[21] T. Shijo,T. Itoh, M. Ando, "Visualization of Physical Optics for Interpretation of High Frequency Phenomena", *URSI 2004 Conference*,2004.